

1       **A Regional multi-Air Pollutant Assimilation System (RAPAS v1.0)**  
2               **for emission estimates: System development and application**

3       Shuzhuang Feng<sup>1</sup>, Fei Jiang<sup>1,2</sup>, Zheng Wu<sup>3</sup>, Hengmao Wang<sup>1,2</sup>, Wei He<sup>1</sup>, Yang Shen<sup>1</sup>,  
4               Lingyu Zhang<sup>1</sup>, Yanhua Zheng<sup>1</sup>, Chenxi Lou<sup>1</sup>, Ziqiang Jiang<sup>4</sup>, Weimin Ju<sup>1,2</sup>

5  
6       <sup>1</sup> *Jiangsu Provincial Key Laboratory of Geographic Information Science and Technology, International*  
7       *Institute for Earth System Science, Nanjing University, Nanjing, 210023, China*

8       <sup>2</sup> *Jiangsu Center for Collaborative Innovation in Geographical Information Resource Development and*  
9       *Application, Nanjing, 210023, China*

10       <sup>3</sup> *Chongqing Institute of Meteorological Sciences, Chongqing, 401147, China*

11       <sup>4</sup> *Jiangsu Environmental Monitoring Center, Nanjing, 210019, China*

12  
13  
14  
15  
16       *Correspondence to: Fei Jiang (jiangf@nju.edu.cn)*

## 30 Abstract

31 Top-down atmospheric inversions ~~infer~~<sub>s</sub> surface-atmosphere fluxes from spatially  
32 distributed observations of atmospheric compositions, ~~which is a vital means for~~  
33 ~~quantifying in order to quantify~~ anthropogenic and natural emissions. In this study, we  
34 developed a Regional multi-Air Pollutant Assimilation System (RAPAS v1.0) based on  
35 the Weather Research and Forecasting/Community Multiscale Air Quality Modelling  
36 System (WRF/CMAQ) model, the three-dimensional variational (3DVAR) algorithm,  
37 and the ensemble square root filter (EnSRF) algorithm. This system can simultaneously  
38 assimilate hourly *in-situ* CO, SO<sub>2</sub>, NO<sub>2</sub>, PM<sub>2.5</sub> and PM<sub>10</sub> observations to infer gridded  
39 emissions of CO, SO<sub>2</sub>, NO<sub>x</sub>, primary PM<sub>2.5</sub> (PPM<sub>2.5</sub>), and coarse PM<sub>10</sub> (PMC) on a  
40 regional scale. In each data assimilation window, we use a “two-step” scheme, in which  
41 the emissions ~~are~~<sub>s</sub> ~~is~~ inferred first, and then input into the CMAQ model to simulate  
42 initial conditions (IC) of the next window. The posterior emissions ~~are~~<sub>s</sub> ~~is~~ transferred to  
43 the next window as the prior emission, and the original emission inventory is only used  
44 in the first window. Additionally, a “super-observation” approach is implemented to  
45 decrease the computational costs, observation error correlations, and influence of  
46 representative errors. Using this system, we estimated the emissions of CO, SO<sub>2</sub>, NO<sub>x</sub>,  
47 PPM<sub>2.5</sub>, and PMC in December and July 2016 over China using nationwide surface  
48 observations. The results showed ~~ed~~ that compared to the prior emissions (MEIC 2016),  
49 the posterior emissions of CO, SO<sub>2</sub>, NO<sub>x</sub>, PPM<sub>2.5</sub>, and PMC in December 2016  
50 increased by 129%, 20%, 5%, 95%, and 1045%, respectively, and the emission  
51 uncertainties decreased by 44%, 45%, 34%, 52%, and 56%, respectively. With the  
52 inverted emissions, the RMSE of simulated concentrations decreased by 40–56%.  
53 Sensitivity tests were conducted with different prior emissions, prior uncertainties, and  
54 observation errors. The results showed that the “two-step” scheme employed in RAPAS  
55 is robust in estimating emissions using nationwide surface observations over China.  
56 This study offers a useful tool for accurately quantifying multi-species anthropogenic  
57 emissions at large scales and in near real time.

58

59 **1. Introduction**

60 Owing to rapid economic development and pollution control legislation, there is an  
61 increasing demand to provide updated emission estimates, especially in areas where  
62 anthropogenic emissions are intensive. Accurately estimating source emission  
63 quantities and spatiotemporal changes resulting from various regulations is imperative  
64 and valuable for understanding air quality responses and is crucial for providing timely  
65 instructions for the design of future emission regulations. However, most inventories  
66 were developed based on a bottom-up approach and are usually updated with a delay  
67 of a few years owing to the complexity of gathering statistical information on activity  
68 levels and sector-specific emission factors (Ding et al., 2015). The large uncertainty  
69 associated with the low temporal and spatial resolutions of these datasets also greatly  
70 limits the assessment of emission changes. Some studies (Bauwens et al., 2020; Shi and  
71 Brasseur, 2020) evaluated emission changes indirectly through concentration  
72 measurements; however, air pollution changes are not only dominated by emission  
73 changes, but also highly affected by meteorological conditions (Shen et al., 2021).

74 Top-down atmospheric inversion infers surface-atmosphere fluxes from spatially  
75 distributed observations of atmospheric compositions. Recent efforts have been focused  
76 on developing air pollution data assimilation (DA) systems to conduct top-down  
77 inversions, which can integrate model and multi-source observational information to  
78 constrain emission sources. Two major methods are widely used in those DA systems:  
79 4D-variational data assimilation (4DVAR) and ensemble Kalman filter (EnKF).  
80 4DVAR provides a global optimal analysis by minimizing a cost function. It shows an  
81 implicit flow-dependent background error covariance and can reflect complex  
82 nonlinear constraint relationships (Lorenc, 2003). Additionally, a weak constraint  
83 4DVAR method can partly account for the model error by defining a systematic error  
84 term in a cost function (Derber, 1989). For example, the GEOS-Chem and TM5 4DVAR  
85 frameworks have been used to estimate CH<sub>4</sub> (Alexe et al., 2015; Monteil et al., 2013;  
86 Schneising et al., 2009; Stanevich et al., 2021; Wecht et al., 2014) and CO<sub>2</sub> fluxes (Basu  
87 et al., 2013; Nassar et al., 2011; Wang et al., 2019a) from different satellite retrieval

88 products. Additionally, Jiang et al. (2017) and Stavrakou et al. (2008) also used the  
89 4DVAR algorithm to estimate global CO and NO<sub>x</sub> emission trends using MOPITT and  
90 GOME/SCIAMACHY retrievals, respectively. Using NIES LiDAR observations,  
91 Yumimoto et al. (2008) applied the 4DVAR DA to infer dust emissions over eastern  
92 Asia and the results agreed well with various satellite data and surface observations.  
93 Based on surface observations, Meirink et al. (2008) developed a 4DVAR system to  
94 optimize monthly methane emissions, which showed a high degree of consistency in  
95 posterior emissions and uncertainties when compared with an analogous inversion  
96 based on the traditional synthesis approach.

97 Although considerable progress has been made to reduce large uncertainties in emission  
98 inventories, the drawback of the 4DVAR method is the additional development of  
99 adjoint models, which are technically difficult and cumbersome for complex chemical  
100 transport models (Bocquet and Sakov, 2013). Instead, EnKF uses flow-dependent  
101 background error covariance generated by ensemble simulations to map deviations in  
102 concentrations to increments of emissions, which is more flexible and easier to  
103 implement. Many previous studies used EnKF techniques to assimilate single- or dual-  
104 species observations to optimize the corresponding emission species (Chen et al., 2019;  
105 Peng et al., 2017; Schwartz et al., 2014; Sekiyama et al., 2010). Miyazaki et al. (2017)  
106 improved NO<sub>x</sub> emission estimates using multi-constituent satellite observations, and  
107 further estimated global surface NO<sub>x</sub> emissions from 2005 to 2014. Feng et al., (2020b)  
108 used surface observations of NO<sub>2</sub> to infer the NO<sub>x</sub> emission changes in China during  
109 the COVID-19, and quantitatively evaluate the impact of the epidemic on economic  
110 activities from the perspective of emission change. Tang et al. (2011) adjusted the  
111 emissions of NO<sub>x</sub> and VOCs through assimilating surface O<sub>3</sub> observations and achieved  
112 an better performance in O<sub>3</sub> forecasts. However, such a revision may encounter the  
113 problem of model error compensation rather than a retrieval of physically meaningful  
114 quantities, which should be avoided from overfitting for emission inversion purposes  
115 (Bocquet, 2012; Navon, 1998; Tang et al., 2011). The EnKF has also been widely  
116 applied to optimize emissions of carbon dioxide (Jiang et al., 2021; Liu et al., 2019),

117 carbon monoxide (Feng et al., 2020a; Mizzi et al., 2018), sulfur dioxide (Chen et al.,  
118 2019), ammonia (Kong et al., 2019), etc.

119 Multi-species data assimilation can efficiently reduce the uncertainty in emission  
120 inventories and has led to improvements in air quality forecasting (Ma et al., 2019;  
121 Miyazaki et al., 2012b) as it offers additional constraints on emission estimates through  
122 improvements in related atmospheric fields, chemical reactions, and gas-particle  
123 transformations (Miyazaki and Eskes, 2013). Barbu et al. (2009) updated sulfur oxide  
124 ( $\text{SO}_x$ ) emissions with  $\text{SO}_2$  and sulfate aerosol observations and found that the  
125 simultaneous assimilation of both species performed better than assimilating them  
126 separately. Muller and Stavrou (2005) also found that the simultaneous optimization  
127 of the sources of CO and  $\text{NO}_x$  led to better agreement between simulations and  
128 observations compared to the case where only CO observations are used.

129 The deviation in the chemical initial conditions (IC) is an important source of error that  
130 affects the accuracy of emission inversion because atmospheric inversion fully  
131 attributes the biases in simulated and observed concentrations to deviations in  
132 emissions (Meirink et al., 2006; Peylin et al., 2005). The biases of concentrations would  
133 be compensated by the unreasonable adjustment of pollution emissions without the  
134 optimization of ICs (Tang et al., 2013). Simultaneously optimizing chemical ICs and  
135 emissions has been applied to constrain emissions in many previous studies (Ma et al.,  
136 2019; Miyazaki et al., 2012a; Peng et al., 2018). For example, Elbern et al. (2007)  
137 adjusted  $\text{O}_3$ ,  $\text{NO}_x$ , and VOCs ICs, and  $\text{NO}_x$  and VOCs emissions. ~~ICs,  $\text{NO}_x$  ICs and~~  
138 ~~emissions, VOCs ICs and emissions~~ jointly through assimilating surface  $\text{O}_3$  and  $\text{NO}_x$   
139 observations. Although the forecast skills of  $\text{O}_3$  were improved, due to the coarse model  
140 resolution and the strong nonlinear relationship between  $\text{O}_3$  and  $\text{NO}_x$ , the assimilation  
141 of  $\text{O}_3$  observation worsened emission inversion and forecast of  $\text{NO}_x$ . Peng et al. (2018)  
142 assimilated near-surface observations to simultaneously optimize the ICs and emissions.  
143 In the 72-hr forecast evaluation, their resultant emission succeeded in improving  $\text{SO}_2$   
144 forecast while having little influence on CO and aerosol forecast and even degrading  
145 the forecast of  $\text{NO}_2$ . Ma et al. (2019) also found that the DA benefits for forecast almost

146 disappeared after 72 hr using optimized ICs and emissions. Although a large  
147 improvement has been achieved, this method has significant limitations in emission  
148 inversion as the contributions from the emissions and chemical ICs to the model's  
149 biases are difficult to distinguish (Jiang et al., 2017). In addition, the constraints of the  
150 chemical ICs with observations in each assimilation window make the emission  
151 inversions between the windows independent. This means that if the emission in one  
152 window is overestimated or underestimated, it cannot be transferred to the next window  
153 for further correction and compensation. Considering the importance of emissions in  
154 chemical field prediction (Bocquet et al., 2015), the rapid disappearance of the DA  
155 benefits seems unrealistic, indicating that simultaneously optimizing chemical ICs and  
156 emissions may result in a systematic bias in the inverted emissions (Jiang et al., 2021).

157 Since 2013, China has deployed an air pollution monitoring network that publishes  
158 nationwide and real-time hourly surface observations. This dataset provides an  
159 opportunity to improve emission estimates using ~~the~~ DA. In this study, a regional multi-  
160 air pollutant assimilation system using 3DVAR and EnKF DA techniques was  
161 constructed to simultaneously assimilate various surface observations (e.g. CO, SO<sub>2</sub>,  
162 NO<sub>2</sub>, O<sub>3</sub>, PM<sub>2.5</sub>, and PM<sub>10</sub>). We adopted a “two-step” method in this system, in which  
163 the ICs of each DA window were simulated using the posterior emissions of the  
164 previous DA window. The capabilities of RAPAS for reanalysis field generation and  
165 emission inversion estimation were also evaluated. The robustness of the system was  
166 investigated with different prior inventories, uncertainty settings of prior emissions, and  
167 observation errors. The remainder of the paper is organized as follows: Section 2  
168 introduces the DA system and observation data, Section 3 describes the experimental  
169 design, Section 4 presents and discusses the results of the system performance and  
170 sensitivity tests, and Section 5 concludes the paper.

## 171 **2. Method and data**

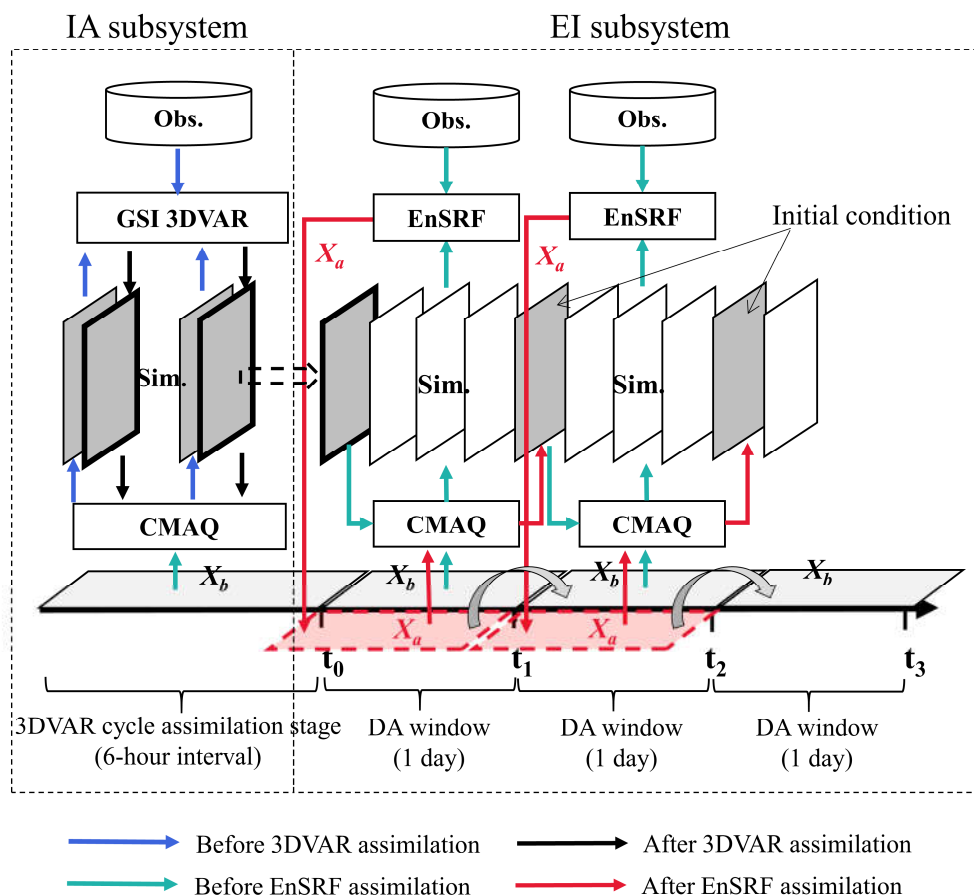
### 172 **2.1 System description**

#### 173 **2.1.1 Procedure of the assimilation system**

174 A regional air pollutant assimilation system has been preliminarily constructed and  
175 successfully applied in our previous studies to optimize the gridded CO and NO<sub>x</sub>  
176 emissions (Feng et al., 2020a; Feng et al., 2020b). Herein, the system was further  
177 extended to simultaneously assimilate multiple species (e.g. CO, SO<sub>2</sub>, NO<sub>2</sub>, O<sub>3</sub>, PM<sub>2.5</sub>,  
178 and PM<sub>10</sub>) and officially named the Regional multi- Air Pollutant Assimilation System  
179 (RAPASv1.0). The RAPAS has three components: a regional chemical transport model  
180 (CTM), which is coupled offline and used to simulate the meteorological fields and  
181 atmospheric compositions, and the 3DVAR and ensemble square root filter (EnSRF)  
182 modules, which are used to optimize chemical ICs (Feng et al., 2018; Jiang et al., 2013b)  
183 and anthropogenic emissions (Feng et al., 2020a; Feng et al., 2020b), respectively.  
184 3DVAR was introduced considering its excellent performance in our previous study and  
185 the lower computational cost during the spin-up period in optimizing ICs. Additionally,  
186 the 3DVAR method can obtain a better IC than the EnKF method (Schwartz et al., 2014).

187 Based on the above three components, the RAPAS was divided into two subsystems:  
188 the IC assimilation (IA) subsystem (CTM plus 3DVAR) and the emission inversion (EI)  
189 subsystem (CTM plus EnSRF). As shown in Figure 1, the IA subsystem was first run  
190 to optimize the chemical ICs (Kleist et al., 2009; Wu et al., 2002) for the subsequent EI  
191 subsystem. Distinguish the source type of model-observation mismatch error was not  
192 required for the IA subsystem. The EI subsystem runs cyclically with a “two-step”  
193 scheme. In the first step, the prior emissions ( $X^b$ ) are perturbed and input into the CTM  
194 model to simulate chemical concentration ensembles. The simulated concentrations of  
195 the lowest model level were then interpolated to the observation space according to the  
196 locations and times of the observations using the nearest-neighbor interpolation method.  
197 Prior emissions ( $X^b$ ), simulated observations and real observations were entered into  
198 the EnSRF module to generate optimized emissions ( $X^a$ ). In the second step, the  
199 optimized emissions were re-entered into the CTM model to generate the ICs of the  
200 next DA window. Meanwhile, the optimized emissions were transferred to the next  
201 window as prior emissions. Unlike joint adjustment of ICs and emissions (“one-step”  
202 scheme) in emission inversion (Chen et al., 2019), the “two-step” scheme needs to run

203 the CTM model twice, which is time consuming but can transfer the potential errors of  
 204 the inverted emissions in one DA window to the next for further correction.



205

206 **Figure 1.** Composition and flow chart of RAPAS.  $\mathbf{x}_a$  and  $\mathbf{x}_b$  represent the prior and  
 207 posterior emissions. The 3DVAR assimilation stage lasts five days with data input  
 208 frequency of six hours and the DA window in the EI subsystem is set to one day.

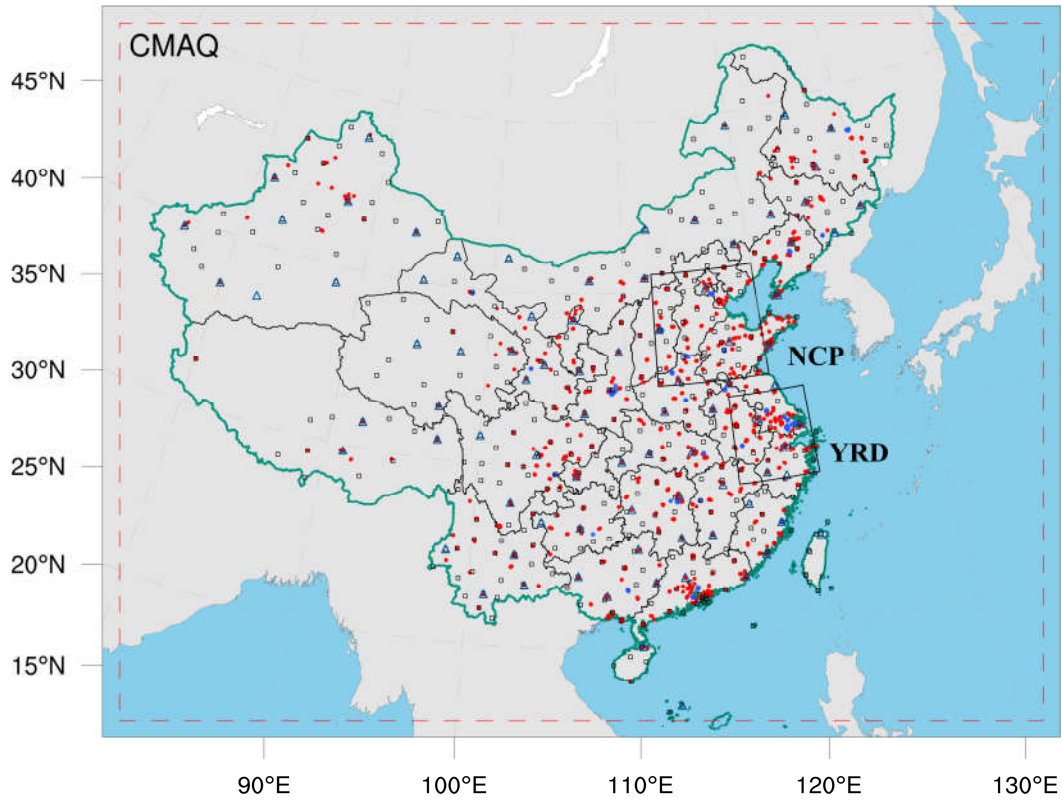
209 **2.1.2 Atmospheric transport model**

210 The regional chemical transport model of the Weather Research and  
 211 Forecasting/Community Multiscale Air Quality Modelling System (WRF/CMAQ) was  
 212 adopted in this study. CMAQ is a regional 3-D Eulerian atmospheric chemistry and  
 213 transport model with a “one-atmosphere” design developed by the US Environmental  
 214 Protection Agency (EPA). It can simultaneously address the complex interactions  
 215 among multiple pollutants/air quality issues. The CMAQ model was driven by the WRF  
 216 model, which is a state-of-the-art mesoscale numerical weather prediction system



217 designed for both atmospheric research and meteorological field forecasting. In this  
218 study, WRF version 4.0 and CMAQ version 5.0.2 were used. The WRF simulations  
219 were performed with a 36-km horizontal resolution on  $169 \times 129$  grids, covering all of  
220 mainland China (Figure 2). This spatial resolution has been widely adopted in regional  
221 simulations as it can provide good simulations of spatiotemporal variations in air  
222 pollutants (Mueller and Mallard, 2011; Sharma et al. 2016). In the vertical direction,  
223 there were 51 sigma levels on the sigma-pressure coordinates extending from the  
224 surface to 100 hPa. The underlying surface of the urban and built-up land was replaced  
225 by the MODIS land cover retrieval of 2016 to adapt to the rapid expansion of  
226 urbanization. The CMAQ model was run with the same domain but with three grid cells  
227 removed from each side of the WRF domain. There were 15 layers in the CMAQ  
228 vertical coordinates, which were interpolated from 51 WRF layers.

229 The meteorological initial and lateral boundary conditions were both provided by the  
230 Final Operational Global Analysis data of the National Center for Environmental  
231 Prediction (NCEP) with a  $1^\circ \times 1^\circ$  resolution at 6-h intervals. The chemical lateral  
232 boundary conditions and chemical ICs in the IA subsystem originate from background  
233 profiles. As mentioned above, in the EI subsystem, the chemical IC in the first window  
234 is provided by the IA subsystem and in the following windows, it is forward simulated  
235 using optimized emissions from the previous window. Carbon Bond 05 with updated  
236 toluene chemistry (CB05tucl) and the 6th generation aerosol module (AERO6) were  
237 chosen as the gas-phase and aerosol chemical mechanisms, respectively (Appel et al.,  
238 2013; Sarwar et al., 2012). The detailed physical and chemical configurations are listed  
239 in Table 1.



240

241 **Figure 2.** Model domain and observation network. The red dashed frame depicts the  
 242 CMAQ computational domain; the black squares represent the surface meteorological  
 243 measurement sites; the navy blue triangles represent the sounding sites; and the red and  
 244 blue dots represent the air pollution measurement sites. Observations from all sites were  
 245 assimilated in the 3DVAR subsystem, while observations of city sites where red dots  
 246 were averaged are used for assimilation and where blue dots were averaged are used  
 247 for independent evaluation in the EI subsystem; the boxed subregions are the North  
 248 China Plain (NCP) and Yangtze River Delta (YRD); and the shaded area depicts the  
 249 topography.

250

251

252

253

254

255 **Table 1.** Configuration options of WRF/CMAQ

WRF		CMAQ	
Parameter	Scheme	Parameter	Scheme
Microphysics	WSM6	Horizontal/Vertical advection	yamo/wrf
Longwave	RRTM	Horizontal/Vertical diffusion	multiscale/acm2
Shortwave	Goddard	Deposition	m3dry
Boundary layer	ACM	Chemistry solver	EBI
Cumulus	Kain-Fritsch	Photolysis	phot_inline
Land-surface	Noah	Aerosol module	AERO6
Surface layer	Revised	Cloud module	cloud_acm_ae6
Urban canopy	No	Gas-phase chemistry	CB05tucl

256 **2.1.3 3DVAR assimilation algorithm**

257 Grid-point Statistical Interpolation (GSI) developed by the US NCEP was utilized in  
 258 this study. Building on the work of Liu et al. (2011), Jiang et al. (2013b) and Feng et al.  
 259 (2018), we extended GSI to simultaneously assimilate multiple species (including CO,  
 260 SO<sub>2</sub>, NO<sub>2</sub>, O<sub>3</sub>, PM<sub>2.5</sub>, and PM<sub>10</sub>) and first used individual aerosol species of PM<sub>2.5</sub> as  
 261 analysis variables within the GSI/WRF/CMAQ framework. Additional work includes  
 262 the construction of surface air pollutant observation operators, the updating of  
 263 observation errors, and the statistics of background error covariance for the analysis  
 264 variables. Moreover, the data interface was modified to read/write the CMAQ  
 265 output/input file directly, which was easy to implement.

266 In the sense of minimum analysis error variance, the 3DVAR algorithm optimizes the  
 267 analysis fields with observations by an iterative processes to minimize the cost function  
 268  $J(\mathbf{x})$  defined below:

$$269 \quad J(\mathbf{x}) = \frac{1}{2}(\mathbf{x}_a - \mathbf{x}_b)^T \mathbf{B}^{-1}(\mathbf{x}_a - \mathbf{x}_b) + \frac{1}{2}[H(\mathbf{x}_a) - \mathbf{y}]^T \mathbf{R}^{-1}[H(\mathbf{x}_a) - \mathbf{y}], \quad (1)$$

270 where  $\mathbf{x}_a$  is a vector of the analysis field,  $\mathbf{x}_b$  is the background field,  $\mathbf{y}$  is the vector  
 271 of observations,  $\mathbf{B}$  and  $\mathbf{R}$  are the background and observation error covariance matrices,

272 respectively, representing the relative contributions to the analysis, and  $H$  is the  
273 observation operator that maps the model variables to the observation space.

274 The analysis variables were the 3D mass concentrations of the pollution components  
275 (e.g. CO and sulfate) at each grid point. Hourly mean surface pollution observations  
276 within a one-hour window of the analysis were assimilated. To assimilate the surface  
277 pollution observations, model-simulated compositions were first diagnosed at  
278 observation locations. For gas concentrations to be directly used as analysis variables,  
279 the units need to be converted from ppm and ppb to  $\text{mg m}^{-3}$  and  $\mu\text{g m}^{-3}$ , respectively, to  
280 match the observations. The model-simulated  $\text{PM}_{2.5}$  and  $\text{PM}_{10}$  concentrations at the  
281 ground level were diagnosed as follows:

$$282 \quad \text{PM}_{2.5} = f_i \times \text{PM}_i + f_j \times \text{PM}_j + f_k \times \text{PM}_k = \text{OC} + \text{EC} + \text{SO}_4^{2-} + \text{NO}_3^- + \text{NH}_4^+ + \\ 283 \quad \text{SEAS} + \text{AP}_{2.5} \quad (2)$$

$$284 \quad \text{PM}_{10} = \text{PM}_i + \text{PM}_j + \text{PM}_k = \text{PM}_{2.5} + \text{PMC} \quad (3)$$

285 where  $f_i$ ,  $f_j$ , and  $f_k$  are the  $\text{PM}_{2.5}$  fractions of the Aitken, accumulation, and coarse  
286 modes, respectively. These ratios are recommended as the concentrations of  $\text{PM}_{2.5}$  and  
287 fine mode aerosols (i.e. Aitken plus accumulation) can differ because  $\text{PM}_{2.5}$  particles  
288 include small tails from the coarse mode in the CMAQ model (Binkowski and Roselle,  
289 2003; Jiang et al., 2006).  $\text{PM}_i$ ,  $\text{PM}_j$ , and  $\text{PM}_k$  are the mass concentrations of the three  
290 modes in the CMAQ model, respectively. Seven aerosol species of  $\text{PM}_{2.5}$  (organic  
291 carbon (OC), elemental carbon (EC), sulfate ( $\text{SO}_4^{2-}$ ), nitrate ( $\text{NO}_3^-$ ), ammonium ( $\text{NH}_4^+$ ),  
292 sea salt (SEAS), and fine-mode unspiciated aerosols ( $\text{AP}_{2.5}$ )) and additional coarse  
293  $\text{PM}_{10}$  (PMC) were extracted as analysis variables and were updated using the  $\text{PM}_{2.5}$  and  
294 PMC observations. Before calculating equation (1) within the GSI, the analysis  
295 variables were bilinearly interpolated in the horizontal direction to the observation  
296 locations.

297 Calculating background error covariance ( $\mathbf{B}$ ) is generally costly and difficult when a  
298 high-dimensional numerical model is used. For simplification,  $\mathbf{B}$  was represented as a

299 product of spatial correlation matrices and standard deviations (SDs).

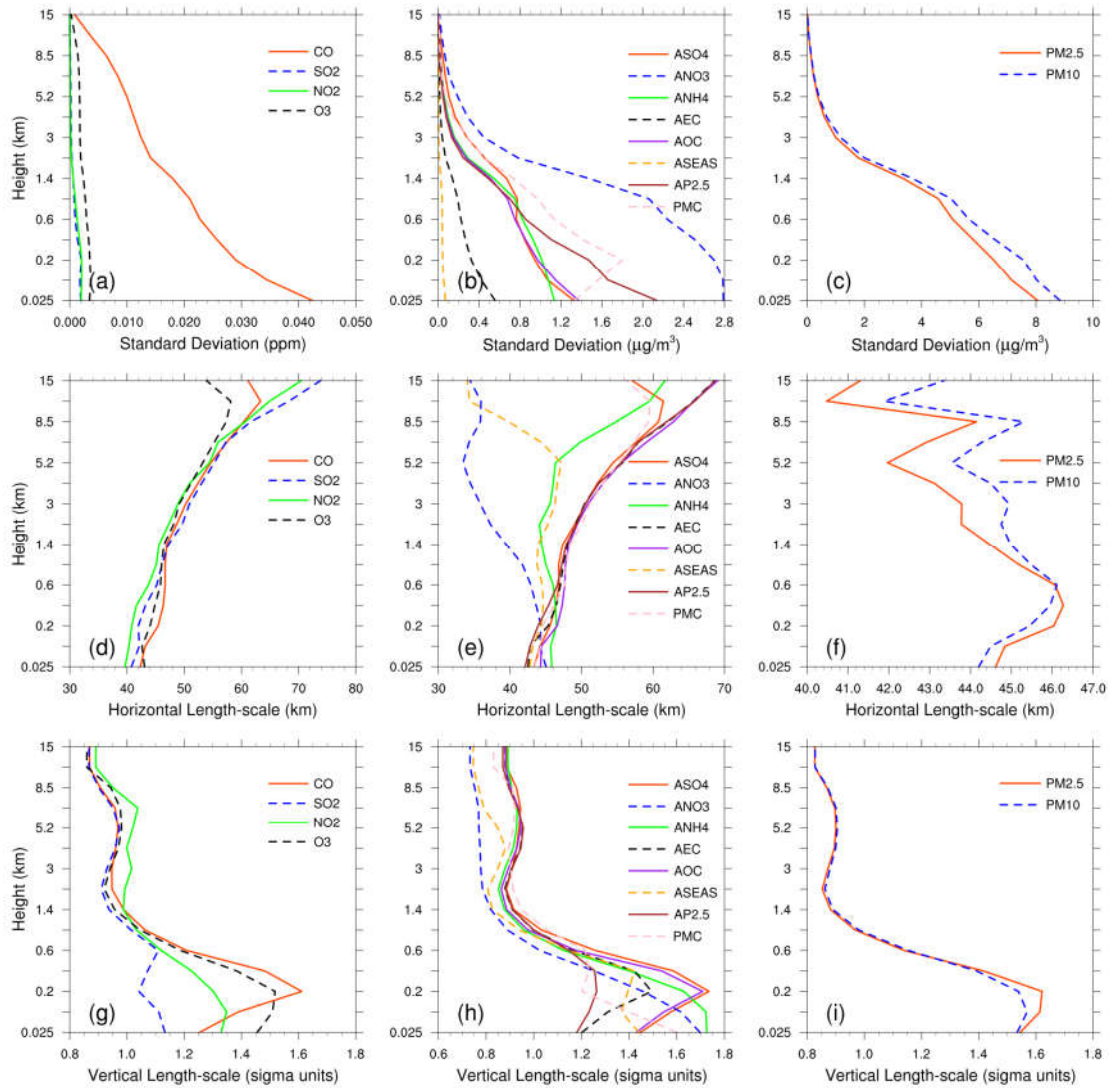
$$300 \quad \mathbf{B} = \mathbf{D}\mathbf{C}\mathbf{D}^T \quad (4)$$

$$301 \quad \mathbf{C} = \mathbf{C}_x \otimes \mathbf{C}_y \otimes \mathbf{C}_z \quad (5)$$

302 where  $\mathbf{D}$  is the background error SD matrix;  $\mathbf{C}$  is the background error correlation  
303 matrix;  $\otimes$  is the Kronecker product; and  $\mathbf{C}_x$ ,  $\mathbf{C}_y$ , and  $\mathbf{C}_z$  denote three one-  
304 dimensional correlation submatrices in the longitude, latitude, and vertical coordinate  
305 directions, respectively.  $\mathbf{C}_x$  and  $\mathbf{C}_y$  are assumed to be horizontally isotropic such that  
306 they can be represented using a Gaussian function. The correlation between any two  
307 points  $x_i$  and  $x_j$  in the horizontal direction is expressed as follows:

$$308 \quad c(x_i, x_j) = e^{-\frac{(x_i-x_j)^2}{2L^2}} \quad (6)$$

309 where  $L$  is the horizontal correlation scale estimated using the proxy of the  
310 background error (Figure 3). The vertical correlation matrix  $\mathbf{C}_z$  is directly estimated  
311 from the model background field as  $\mathbf{C}_z$  is only an  $n_z \times n_z$  (here,  $n_z=15$ ) matrix.



312

313 **Figure 3.** Vertical profiles of standard deviations (top,  $\mu\text{g m}^{-3}$ ), horizontal (middle, km)  
 314 and vertical (bottom, km) length scales for CO, SO<sub>2</sub>, NO<sub>2</sub>, O<sub>3</sub>, sulfate, nitrate,  
 315 ammonium, EC, OC, sea salt, unspciated aerosols (AP2.5), PMC, PM<sub>2.5</sub> and PM<sub>10</sub>.

316 To estimate these matrices, the “NMC” method was used to compute **B** for each variable  
 317 by taking the differences between forecasts of different lengths valid at the same time  
 318 (Parrish and Derber, 1992; Rabier et al., 1998). Differences between the 24- and 12-h  
 319 WRF/CMAQ forecasts of 60 pairs (two pairs per day) of analysis variables valid at  
 320 either 0000 or 1200 UTC over November 2016 were used. The horizontal and vertical  
 321 length scales of the correlation matrices were estimated using recursive filters (Purser  
 322 et al., 2003). The vertical distribution of the background error SDs, which varies with  
 323 height and species, is shown in Figure 3. The vertical profile of the background error

324 SDs corresponds to the vertical concentration distribution. This means that higher  
325 concentrations tend to have larger background error SDs (e.g., CO and nitrate). These  
326 SDs exhibit a common reduction as the height increases, especially at the top of the  
327 boundary layer. The horizontal correlation of the background error determines the  
328 propagation of observation information in this direction, whereas the vertical  
329 correlation determines the vertical extension of such increments. For gaseous pollutants  
330 and most individual aerosol components, the horizontal length scales increased with  
331 height, whereas for the total particulate matter (i.e. PM<sub>2.5</sub>, PM<sub>10</sub>), the scales increased  
332 with height in the boundary layer and decreased with height in the free troposphere.  
333 The ground-level scale generally spread 40–45 km for all control variables. The vertical  
334 length scale of most species first increased and then decreased with height, which may  
335 be related to vertical mixing (Kahnert, 2008) and stack emissions at approximately 200  
336 m height.

#### 337 **2.1.4 EnKF assimilation algorithm**

338 In EnKF, the time-dependent uncertainties of the state variables are estimated using a  
339 Monte Carlo approach through an ensemble. Uncertainty can be propagated using linear  
340 or nonlinear dynamic models (flow-dependent background error covariance) by simply  
341 implementing ensemble simulations. The EnSRF algorithm introduced by Bierman  
342 (1977) and Maybeck (1979) was used to constrain pollution emissions in this study.  
343 EnSRF is a deterministic EnKF that obviates the need to perturb observations, which  
344 has a higher computational efficiency and a better performance (Sun et al., 2009).

345 The perturbation of the prior emissions represents the uncertainty. We implemented  
346 additive emission adjustment methods, which were calculated using the following  
347 function:

$$348 \quad \mathbf{X}_i^b = \mathbf{X}_0^b + \delta\mathbf{X}_i^b, i = 1, 2, \dots, N \quad (7)$$

349 where  $\mathbf{b}$  is the background (prior) state,  $i$  is the identifier of the perturbed samples,  
350 and  $N$  is the ensemble size, which was set to 40 considering the trade-off between  
351 computational cost and inversion accuracy (Figure S1). In contrast to the estimation of

352 parameters based on the augmentation of the conventional state vector (e.g.  
353 concentrations) with the parameter variables,  $\mathbf{X}$  only comprises emissions in this study  
354 (similarly hereafter).  $\delta\mathbf{X}_i^b$  is the randomly perturbed samples added to the prior  
355 emissions  $\mathbf{X}_0^b$  to produce ensemble samples of the inputs  $\mathbf{X}_i^b$ .  $\delta\mathbf{X}_i^b$  is drawn from  
356 Gaussian distributions with a mean of zero and standard deviation of the prior emission  
357 uncertainty in each grid. The state variables of the emissions include CO, SO<sub>2</sub>, NO<sub>x</sub>,  
358 primary PM<sub>2.5</sub> (PPM<sub>2.5</sub>) and PMC. We used variable localization to update the analysis,  
359 which means that the covariance among different state variables was not considered,  
360 and the emission of one species was constrained only by its corresponding air pollutant  
361 observation. This method has been widely used in chemical data assimilation systems  
362 to avoid spurious correlations between species (Ma et al., 2019; Miyazaki et al., 2012b).  
363 After obtaining an ensemble of state vectors (prior emissions), ensemble runs of the  
364 CMAQ model were conducted to propagate the errors in the model with each ensemble  
365 sample of state vectors. Combined with the observational vector  $\mathbf{y}$ , the state vector  $\overline{\mathbf{X}}^b$   
366 was updated by minimizing the analysis variance.

$$367 \quad \overline{\mathbf{X}}^a = \overline{\mathbf{X}}^b + \mathbf{K}(\mathbf{y} - \mathbf{H}\overline{\mathbf{X}}^b) \quad (8)$$

$$368 \quad \mathbf{K} = \mathbf{P}^b \mathbf{H}^T (\mathbf{H} \mathbf{P}^b \mathbf{H}^T + \mathbf{R})^{-1} \quad (9)$$

$$369 \quad \mathbf{P}^b = \frac{1}{N-1} \sum_{i=1}^N (\mathbf{X}_i^b - \overline{\mathbf{X}}^b) (\mathbf{X}_i^b - \overline{\mathbf{X}}^b)^T \quad (10)$$

$$370 \quad \delta\mathbf{X}_i^a = \delta\mathbf{X}_i^b - \tilde{\mathbf{K}} \mathbf{H} \delta\mathbf{X}_i^b \quad (11)$$

371 While employing sequential assimilation and independent observations,  $\tilde{\mathbf{K}}$  is  
372 calculated as follows:

$$373 \quad \tilde{\mathbf{K}} = \left(1 + \sqrt{\mathbf{R}/(\mathbf{H} \mathbf{P}^b \mathbf{H}^T + \mathbf{R})}\right)^{-1} \mathbf{K} \quad (12)$$

374 where  $\overline{\mathbf{X}}^b$  is the mean of the ensemble samples  $\mathbf{X}_i^b$ ;  $\mathbf{H}$  is the observation operator that  
375 maps the model space to the observation space, consisting of the model integration



376 process converting emissions into concentrations and spatial interpolation matching the  
 377 model concentration to the locations of the observations;  $\mathbf{y} - \mathbf{H}\overline{\mathbf{X}}^b$  reflects the  
 378 differences between the simulated and observed concentrations;  $\mathbf{P}^b$  is the ensemble-  
 379 estimated background (a priori) error covariance;  ~~$\mathbf{P}^b \mathbf{H}^T$  contains the response of the~~  
 380 ~~uncertainty in the simulated concentrations to the uncertainty in emissions;~~  $\mathbf{K}$  is the  
 381 Kalman gain matrix of the ensemble mean depending on the background error  
 382 covariance  $\mathbf{P}^b$  and the observation error covariance  $\mathbf{R}$ , representing the relative  
 383 contributions to analysis; and  $\tilde{\mathbf{K}}$  is the Kalman gain matrix of the ensemble  
 384 perturbation, which is used to calculate emission perturbations after inversions  $\delta\mathbf{X}_i^a$ .  
 385 The ensemble mean  $\overline{\mathbf{X}}^a$  of the analyzed state was considered the best estimate of the  
 386 emissions.

387 When large volumes of site observations are at a much higher resolution than the model  
 388 grid spacing, many correlated or fully consistent model-data mismatch errors can  
 389 appear in one cluster, resulting in excessive adjustments and deteriorated model  
 390 performance (Houtekamer and Mitchell, 2001). To reduce the horizontal observation  
 391 error correlations and influence of representativeness errors, a “super-observation”  
 392 approach combining multiple noisy observations located within the same grid and  
 393 assimilation window was developed based on optimal estimation theory (Miyazaki et  
 394 al., 2012a). Previous studies demonstrated the necessity for data-thinning and  
 395 dealiasing errors (Feng et al., 2020b; Zhang et al., 2009a). The super-observation  $y_{new}$ ,  
 396 super-observation error  $r_{new}$ , and corresponding simulation  $x_{new,i}$  of the  $i$ th sample  
 397 are calculated as follows:

$$398 \quad 1/r_{new}^2 = \sum_{j=1}^m 1/r_j^2 \quad (13)$$

$$399 \quad y_{new} = \sum_{j=1}^m w_j y_j / \sum_{j=1}^m w_j \quad (14)$$

$$400 \quad x_{new,i} = \sum_{j=1}^m w_j x_{ij} / \sum_{j=1}^m w_j \quad (15)$$

401 where  $j$  is the identifier of  $m$  observations within a super-observation grid;  $r_j$  is the

402 observational error of the actual  $j$ th observation  $y_j$ ;  $x_{ij}$  is the simulated concentration  
403 using the  $i$ th prior emission sample corresponding to the  $j$ th observation; and  $w_j =$   
404  $1/r_j^2$  is the weighting factor. The super-observation error decreased as the number of  
405 observations used within a super-observation increased. This method was used in our  
406 previous inversions using surface-based (Feng et al., 2020b) and satellite-based (Jiang  
407 et al., 2021) observations.

408 In this study, the DA window was set to one day because the model requires a longer  
409 time to integrate the emission information into the concentration ensembles (Ma et al.,  
410 2019). Due to the “super-observation” approach, only one assimilation is needed per  
411 grid cell in one assimilation window. In addition, owing to the complexity of hourly  
412 emissions, it is difficult to simulate hourly concentrations that match the observations  
413 well. Although a longer DA window would allow more observations to constrain the  
414 emission change of one grid, the spurious correlation signals of EnKF would attenuate  
415 the observation information over time (Bruhwiler et al., 2005; Jiang et al., 2021). Kang  
416 et al. (2012) conducted OSSEs and demonstrated that owing to the transport errors and  
417 increased spurious correlation, a longer DA window (e.g. 3 weeks) would cause the  
418 analysis system to blur essential emission information away from the observation.  
419 Therefore, daily mean simulations and observations were used in the EnSRF algorithm  
420 and daily emissions were optimized in this system.

421 EnKF is subject to spurious correlations because of the limited number of ensembles  
422 when it is applied in high-dimensional atmospheric models, which can cause rank  
423 deficiencies in the estimated background error covariance and filter divergence and  
424 further degrade analyses and forecasts (Wang et al., 2020). Covariance localization is  
425 performed to reduce spurious correlations caused by a finite ensemble size  
426 (Houtekamer and Mitchell, 2001). Covariance localization preserves the meaningful  
427 impact of observations on state variables within a certain distance (cutoff radius) but  
428 limits the detrimental impact of observations on remote state variables. The localization

429 function of Gaspari and Cohn ~~function~~ (Gaspari and Cohn, 1999) is used in this system,  
430 which is a piecewise continuous fifth-order polynomial approximation of a normal  
431 distribution. The optimal localization scale is related to the ensemble size, assimilation  
432 window, dynamic system, and lifetime of the chemical species in the atmosphere. CO,  
433 SO<sub>2</sub> and PM<sub>2.5</sub> are rather stable in the atmosphere, with a lifetime of more than one day.  
434 According to the average wind speed (3.3 m/s, Table 4) and length of the DA window,  
435 the localization scales of CO, SO<sub>2</sub> and PM<sub>2.5</sub> were set to 300 km. In addition, the  
436 localization scales of NO<sub>2</sub>, which is rather reactive and has a lifetime of approximately  
437 10 hours in winter (de Foy et al., 2015), and PMC, which mainly comes from local  
438 sources and has a short residence time in the atmosphere owing to the rapid deposition  
439 rate (Clements et al., 2014; Clements et al., 2016; Hinds, 1982), were set to 150 and  
440 250 km, respectively.

## 441 **2.2 Prior emissions and uncertainties**

442 Anthropogenic emissions over China were obtained from the 2016 Multi-resolution  
443 Emission Inventory for China (MEIC 2016) (Zheng et al., 2018), while those over the  
444 other regions of East Asia were obtained from the mosaic Asian anthropogenic emission  
445 inventory (MIX) (Li et al., 2017). The spatial resolutions of the MEIC and MIX  
446 inventories were both 0.25° × 0.25° and they are downscaled to match the model grid  
447 spacing of 36 km. The spatial distributions of CO, SO<sub>2</sub>, NO<sub>x</sub>, PPM<sub>2.5</sub>, and PMC  
448 emissions are shown in Figure 11. The daily emission inventory, which was  
449 arithmetically averaged from the combined monthly emission inventory, was directly  
450 used in the EI subsystem and was employed as the prior emission of the first DA  
451 window in the EI subsystem (Figure 1). During the simulations, daily emissions were  
452 further converted to hourly emissions. All species emitted from area sources were  
453 converted to hourly emissions using the same diurnal profile (Figure S2) and for the  
454 point source, we assumed that there was no diurnal change. MEIC 2012 was used as an  
455 alternative a priori over China to investigate the impact of different prior emissions on  
456 optimized emissions. The Model of Emissions of Gases and Aerosols from Nature  
457 (MEGAN) (Guenther et al., 2012) was used to calculate time-dependent biogenic

458 emissions, which was driven by the WRF model. Biomass burning emissions were not  
459 included because they have little impact across China during the study period (Zhang  
460 et al., 2020).

461 During the inversion cycles, inverted emissions of different members converge  
462 gradually, and the ensemble-estimated error covariance matrix is likely to be  
463 underestimated. To avoid this, considering the compensation of model errors and  
464 comparable emission uncertainties from one day to the next, we imposed the same  
465 uncertainty on emissions at each DA window. As mentioned above, the optimized  
466 emissions of the current DA window were transferred to the next DA window as prior  
467 emissions. The technology-based emission inventory developed by Zhang et al. (2009b),  
468 using the same method as MEIC, showed that the emissions of PMC and PPM<sub>2.5</sub> had  
469 the largest uncertainties, followed by CO, and finally SO<sub>2</sub> and NO<sub>x</sub>. Therefore, the  
470 uncertainties of PMC, PPM<sub>2.5</sub>, CO, SO<sub>2</sub>, and NO<sub>x</sub> in this study were set as 40%, 40%,  
471 30%, 25%, and 25%, respectively. However, previous studies have shown that inversely  
472 estimated CO and PMC emissions can exceed 100% higher than the bottom-up  
473 emissions (MEIC) in certain areas (Feng et al., 2020b; Ma et al., 2019). Therefore,  
474 according to the extent of underestimation, we set an uncertainty of 100% for both the  
475 CO and PMC emissions at the beginning of the three DA windows to quickly converge  
476 the emissions. Mean emission analysis is generally minimally sensitive to the  
477 uncertainty setting in the assimilation cycle method (Feng et al., 2020; Gurney et al.,  
478 2004; Miyazaki et al., 2012a) as the inversion errors of the current window can be  
479 transferred to the next window for further optimization (Section 4.3).

### 480 **2.3 Observation data and errors**

481 Hourly averaged surface CO, SO<sub>2</sub>, NO<sub>2</sub>, O<sub>3</sub>, PM<sub>2.5</sub>, and PM<sub>10</sub> observations from 1504  
482 national control air quality stations were assimilated into this system, which were  
483 obtained from the Ministry of Ecology and Environment of the People's Republic of  
484 China (<http://106.37.208.233:20035/>, last access: 25 June 2020). These sites are  
485 distributed over most of central and eastern China and become denser near metropolitan  
486 areas (see Figure 2). To ensure data quality, value-range checks were performed to

487 eliminate unrealistic or unrepresentative observations and only the observations within  
488 the subjectively selected threshold range were assimilated (Table 2). In additionally, a  
489 time-continuity check was performed to eliminate gross outliers and sudden anomalies  
490 using the function of  $\max(|O(t) - O(t \pm 1)|) \leq f(t)$ , where  $O(t)$  and  $O(t \pm 1)$   
491 represent observations at time  $t$  and  $t \pm 1$ , respectively, and  $f(t) = T_a + T_b \times O_t$ .  
492 This means that the concentration difference between time  $t$  and time  $t+1$  and  $t-1$  should  
493 be less than  $f(t)$ .  $T_b$  was fixed at 0.15 and the section of  $T_a$  is given in Table 2,  
494 which was determined empirically according to the time series change of concentration  
495 at each site. To avoid potential cross-correlations, we assimilated  $PM_{2.5}$  and PMC.  
496 Additionally, in the EI subsystem, the observations within each city were averaged to  
497 reduce the data density, reduce the error correlation, and increase spatial representation  
498 (Houtekamer and Mitchell, 2001; Houtekamer and Zhang, 2016). Finally, 336 city sites  
499 were available across mainland China, in which data from 311 cities were selected for  
500 assimilation and the remaining 25 were selected for independent validation (Figure 2).  
501 In the IA subsystem, owing to the small horizontal correlation scale (Figure 3), all site  
502 observations were assimilated to provide a good IC for the next emission inversion to  
503 obtain more extensive observation constraints.

504 The observation error covariance matrix ( $\mathbf{R}$ ) includes both the measurement and  
505 representation errors. The measurement error  $\varepsilon_0$  is defined as follows:

$$506 \quad \varepsilon_0 = ermax + ermin \times \Pi_0 \quad (16)$$

507 where  $ermax$  is the base error and  $\Pi_0$  denotes the observed concentration. These  
508 parameters for different species are listed in Table 2 and were determined according to  
509 Chen et al. (2019), Feng et al. (2018), and Jiang et al. (2013b).

510 The representative error depends on the model resolution and characteristics of the  
511 observation locations, which were calculated using the equations of Elbern et al. (2007),  
512 defined as follows:

$$513 \quad \varepsilon_r = \gamma \varepsilon_0 \sqrt{\Delta l / L} \quad (17)$$

514 where  $\gamma$  is a tunable parameter (here,  $\gamma=0.5$ ),  $\Delta l$  is the grid spacing (36 km), and  $L$   
 515 is the radius (3 km for simplification) of the influence area of the observation. The total  
 516 observation error ( $r$ ) was defined as follows:

$$517 \quad r = \sqrt{\varepsilon_0^2 + \varepsilon_r^2} \quad (18)$$

518 **Table 2.** Parameters of quality control and measurement error

Parameter	CO mg m <sup>-3</sup>	SO <sub>2</sub> μg m <sup>-3</sup>	NO <sub>2</sub> μg m <sup>-3</sup>	O <sub>3</sub> μg m <sup>-3</sup>	PM <sub>2.5</sub> μg m <sup>-3</sup>	PMC μg m <sup>-3</sup>
value-range	0.1-12	1-800	1-250	1-250	1-800	1-900
time-continuity ( $T_a$ )	2.5	160	70	80	180	180
ermax	0.05	1	1	1	1.5	1.5
ermin	0.5%	0.5%	0.5%	0.5%	0.75%	0.75%

519

### 520 **3 Experimental design**

521 RAPAS inversions ~~were~~ conducted according to the procedure and settings described  
 522 in Section 2. December is one of the months with the most severe air pollution, whereas  
 523 July is one of the least polluted months in China. Therefore, this study mainly tested  
 524 the performance of the RAPAS system over these two months. For December, the IA  
 525 subsystem was run from 26 November to 31, 2016, with a 6-hour interval cycling  
 526 assimilation to optimize ICs (ICDA). A better IC at 0000 UTC on 1 December could be  
 527 obtained by a five-day high-frequency cycling assimilation and atmospheric mixing.  
 528 The EI subsystem was then run for December 2016 with a one-day assimilation window  
 529 to optimize emissions (EMDA). In July, the system operated identically to that of  
 530 December. It should be noted that owing to the stronger atmospheric oxidation, the  
 531 lifetime of NO<sub>2</sub> in July was significantly shorter than that in December; thus, we  
 532 adopted a smaller localization scale for NO<sub>2</sub> (80 km). Both assimilation experiments  
 533 used the combined prior emission inventories of 2016, as described in Section 2.2, and  
 534 the emission base year coincided with the research stage. An Observing Systems

535 Simulation Experiment (OSSE) was conducted to evaluate the performance of the  
536 RAPAS system, which has been widely used in previous assimilation systems  
537 development (Daley, 1997). In the OSSE experiment, we used the MEIC 2016  
538 inventory as a “true” emission and reduced by 30% over mainland China as a prior  
539 emission. The simulations were ~~simulated~~performed using the “true” emission and  
540 sampled according to the locations and times of the real observations used as artificial  
541 observations. The observation errors were the same as those in EMDA. To evaluate the  
542 IC improvements from the IA subsystem, an experiment without 3DVAR (NODA) was  
543 conducted with the same meteorological fields and physical and chemistry  
544 parameterization settings as those of the ICDA. To evaluate the posterior emissions of  
545 the EI subsystem, two parallel forward modelling experiments were performed for  
546 December 2016: a control experiment (CEP) with prior (MEIC 2016) emissions and a  
547 validation experiment (VEP) with posterior emissions. Both experiments used the same  
548 IC at 0000 UTC on December 01 generated through the IA subsystem. The only  
549 difference between CEP and VEP were emissions. Table 3 summarizes the different  
550 emission inversion experiments conducted in this study.

551 To investigate the robustness of our system, ~~eight~~seven sensitivity tests (from EMS1  
552 to EMS7; see Table 3) were performed. These experiments were all based on EMDA.  
553 EMS1 used MEIC 2012 as the original prior emission in China, aiming to investigate  
554 the impact of different prior inventories on the estimates of emissions. The other  
555 experiments (EMS2–5) aimed to test the impact of different prior uncertainty settings,  
556 in which the prior uncertainties were reduced by -50% and -25%, and increased by 25%  
557 and 50%, respectively. EMS6 aimed to evaluate the impact of observation errors on  
558 emission estimates, in which all observation errors are magnified twice. EMS7 aimed  
559 to evaluate the impact of IC optimization of the first window on emission estimates, in  
560 which the ICs were taken from a five-day spin-up simulation. Eight forward modelling  
561 experiments (VEP1, VEP2, ..., VEP7) were also performed with the posterior  
562 emissions of EMS1 to EMS7 to evaluate their performance.

563

564 **Table 3.** Emission inversion and sensitivity experiments conducted in this study

Exp. Type	Exp. Name	Period	IC of the first DA Window	ICs of the subsequent DA window	Emission
Assimilation	EMDA	1–31 December	0000 UTC on December 1, taken from ICDA	Forecast with posterior emissions in the previous window	MEIC 2016 for December (the first DA window), optimized emissions of the previous window (other DA windows)
	OSSE	1–31 December	Same as EMDA	Same as EMDA	Same as EMDA but with a decrease of 30% for CO, SO <sub>2</sub> , NO <sub>x</sub> , PPM <sub>2.5</sub> , and PMC
Sensitivity	EMS1	1–31 December	Same as EMDA	Same as EMDA	Same as EMDA but for EMIC 2012
	EMS2-5	1–31 December	Same as EMDA	Same as EMDA	Same as EMDA but with a ± 25% or ± 50% of default uncertainty
	EMS6	1–31 December	Same as EMDA	Same as EMDA	Same as EMDA but with a +100% of default observation errors
	EMS7	1–31 December	0000 UTC on December 1, taken from ICNO	Same as EMDA	Same as EMDA

565

566 **4 Results**567 **4.1 Evaluations**568 **4.1.1 Simulated meteorological fields**

569 In the RAPAS system, the inversion approach attributes all biases between the  
570 simulated and observed concentrations to emissions. Meteorological fields dominate  
571 the physical and chemical processes of air pollutants in the atmosphere, and thus their



572 simulation accuracy would significantly affect the estimates of emissions in this study.  
573 To quantitatively evaluate the performance of the WRF simulations, the mean bias  
574 (BIAS), root mean square error (RMSE), and correlation coefficient (CORR) were  
575 calculated against the surface meteorological observations measured at 400 stations and  
576 the planetary boundary layer height (PBLH) was calculated using the sounding data at  
577 92 sites. Surface observations were obtained from the National Climate Data Center  
578 integrated surface database (<http://www.ncdc.noaa.gov/oa/ncdc.html>, last access: 25  
579 October 2021) and sounding data were obtained from the website of the University of  
580 Wyoming (<http://weather.uwyo.edu/upperair/sounding.html>, last access: 10 March  
581 2022). The sounding data had a 12 hour interval. The observed PBLH was calculated  
582 using sound data via the bulk Richardson number method (Richardson et al., 2013).  
583 The spatial distribution of meteorological stations is shown in Figure 2. The simulated  
584 temperature at 2 m (T2), relative humidity at 2 m (RH2), wind speed at 10 m (WS10),  
585 and PBLH from 26 November to 31 December 2016 were evaluated against the  
586 observations. Table 4 summarizes the statistical results of the evaluation of the  
587 simulated meteorological parameters. Overall, T2, RH2 and PBLH were slightly  
588 underestimated, with biases of -0.1 °C, -3.8%, and -41.1 m, respectively. CORRs were  
589 approximately 0.98 for T2, 0.94 for RH2, and 0.90 for PBLH, showing good  
590 consistency between the observations and simulations. WS10 was overestimated, with  
591 a bias of 0.7 m/s and an RMSE of 0.8 m/s, but were better than the simulations from  
592 many previous studies (Chen et al., 2016; Jiang et al., 2012a; Jiang et al., 2012b).  
593 Therefore, the WRF can generally reproduce meteorological conditions sufficiently in  
594 terms of their temporal variation and magnitude over China, which is adequate for our  
595 inversion estimation.

596

597

598

599

600 **Table 4.** Statistics comparing the simulated and observed 10-m wind speed (WS10), 2-  
 601 m temperature (T2), and 2-m relative humidity (RH2), and planetary boundary layer  
 602 height (PBLH).

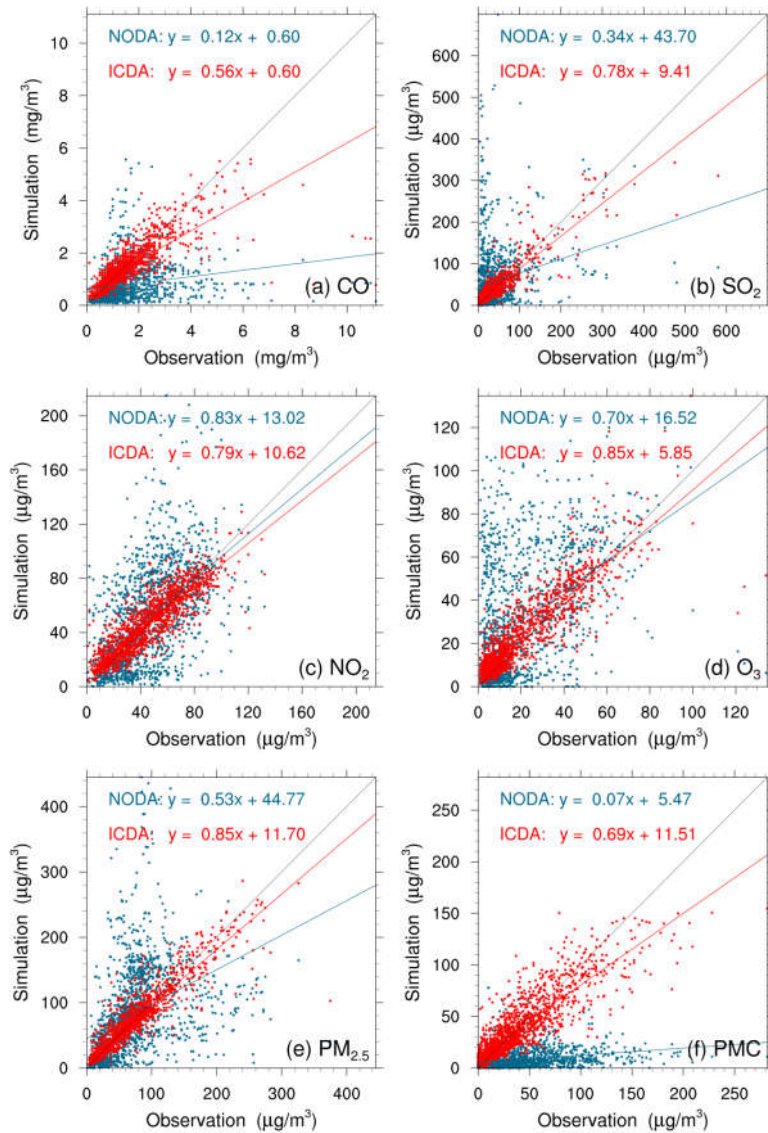
Variable Met.	No. of sites	Mean Obs.	Mean Sim.	BIAS	RMSE	CORR
WS10 (m/s)	400	2.6	3.3	0.7	0.8	0.72
T2 (°C)	400	2.9	2.8	-0.1	0.7	0.98
RH2 (%)	400	66.3	62.6	-3.8	5.2	0.94
PBLH (m)	92	267.5	226.4	-41.1	50.4	0.90

603 \* BIAS, mean bias; RMSE, root mean square error; CORR, correlation coefficient

#### 604 4.1.2 Initial conditions

605 Figure 4 shows an evaluation of the analyzed concentrations of the six species against  
 606 surface observations. For comparison, the evaluations of the simulations without  
 607 3DVAR (NODA) are also shown in Figure 4. The simulations of the NODA experiment  
 608 (red dots) are scattered on both sides of the central line, as large systematic biases  
 609 remain across many measurement sites. Conversely, the ICDA experiment (blue dots)  
 610 showed a much better agreement with the observations than those from NODA. The  
 611 statistics show that there are large systematic biases in the NODA simulations, with  
 612 large RMSEs and small CORRs for all species, particularly for CO and PMC. After the  
 613 assimilation of surface observations, the RMSE of CO decreased to  $0.7 \text{ mg m}^{-3}$ , and  
 614 those of  $\text{SO}_2$ ,  $\text{NO}_2$ ,  $\text{O}_3$ ,  $\text{PM}_{2.5}$ , and PMC decrease to 22.0, 12.0, 9.6, 20.5, and  $19.6 \mu\text{g}$   
 615  $\text{m}^{-3}$ , respectively, with respective reductions of 50.0%, 73.1%, 61.0%, 64.7%, 69.5%,  
 616 and 60.8% compared to those of the NODA (Table 5). The CORRs of ICDA increased  
 617 by 290.0%, 291.3%, 55.4%, 87.2%, 130.0%, and 214.8% to 0.78, 0.90, 0.87, 0.88, 0.92,  
 618 and 0.85, respectively. These statistics indicate that the ICs of the ground level  
 619 improved significantly. However, owing to the lack of observations, we still do not  
 620 know the simulation bias in the upper-middle boundary layer. Although concentrations  
 621 at high altitudes can be constrained by ground-based observations through vertical

622 correlations, the effect is limited; therefore, the bias remains non-negligible.



623

624 **Figure 4.** Scatter plots of simulated versus observed (a) CO, (b) SO<sub>2</sub>, (c) NO<sub>2</sub>, (d) O<sub>3</sub>,  
625 (e) PM<sub>2.5</sub>, and (f) PMC mass concentrations at 0000 UTC on December 1 initializations  
626 from the background (red) and analysis (blue) fields.

627

628

629

630

631

632 **Table 5.** Comparisons of the surface CO, SO<sub>2</sub>, NO<sub>2</sub>, O<sub>3</sub>, PM<sub>2.5</sub>, and PMC mass  
 633 concentrations from the control and assimilation experiment against observations  
 634 aggregated over all analysis times. CO unit: mg m<sup>-3</sup>; others units: µg m<sup>-3</sup>.

Species	Exp. Name	Mean Obs.	Mean Sim.	BIAS	RMSE	CORR
CO	NODA	1.5	0.8	-0.7	1.4	0.20
	ICDA		1.5	-0.1	0.7	0.78
SO <sub>2</sub>	NODA	36.3	56.0	19.7	81.7	0.23
	ICDA		37.8	1.5	22.0	0.90
NO <sub>2</sub>	NODA	45.8	51.1	5.3	30.8	0.56
	ICDA		47.0	1.1	12.0	0.87
O <sub>3</sub>	NODA	20.5	30.8	10.4	27.2	0.47
	ICDA		23.3	2.8	9.6	0.88
PM <sub>2.5</sub>	NODA	70.9	82.2	11.3	67.3	0.40
	ICDA		71.8	0.9	20.5	0.92
PMC	NODA	43.5	8.5	-35.0	50.0	0.27
	ICDA		41.6	-1.9	19.6	0.85

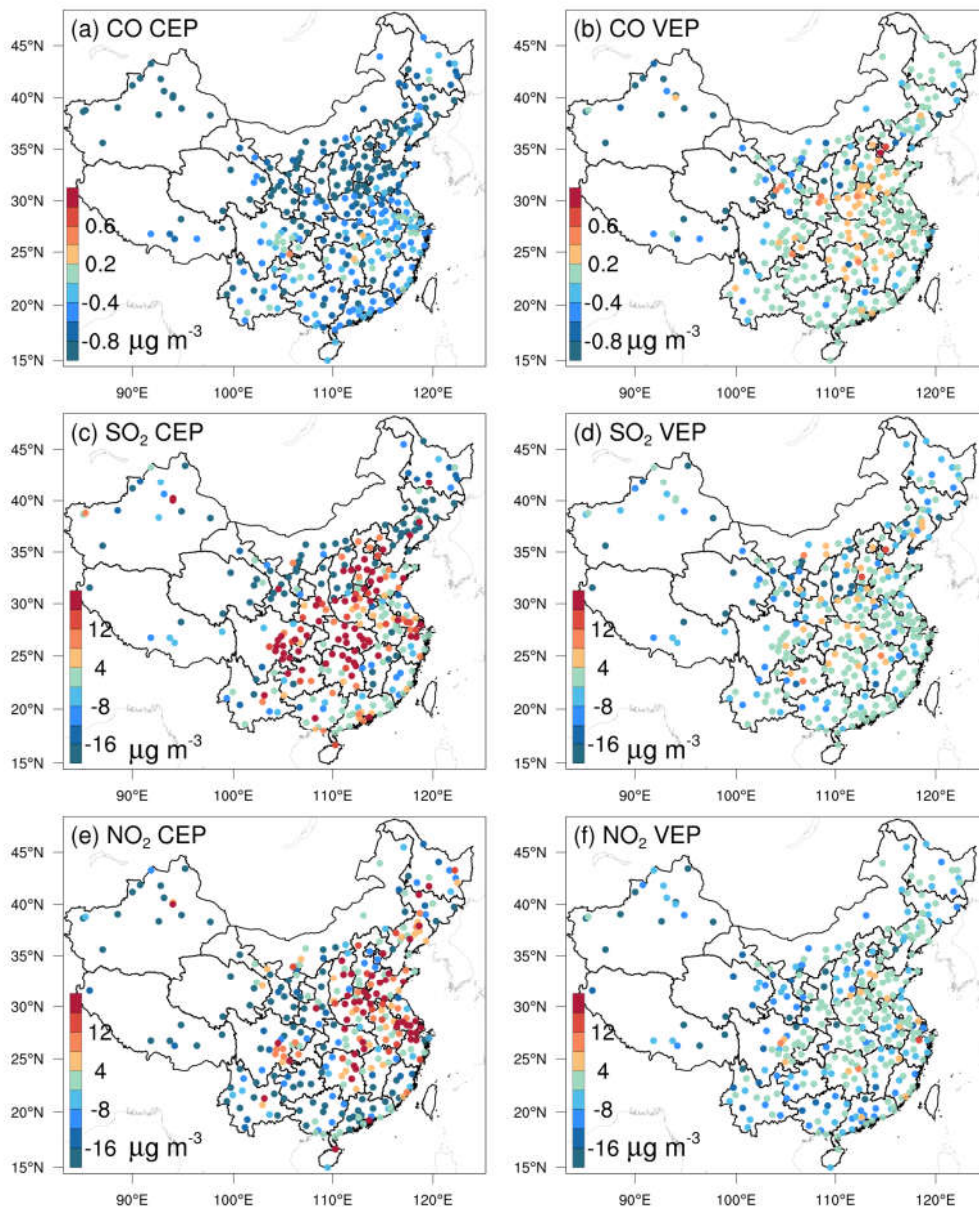
635 \* BIAS, mean bias; RMSE, root mean square error; CORR, correlation coefficient

### 636 4.1.3 Posterior emissions

637 Owing to the mismatched spatial scales, it is difficult to directly evaluate the optimized  
 638 emissions against observations. Generally, we indirectly validated the optimized  
 639 emissions by comparing the forward simulated concentrations using the posterior  
 640 emissions against atmospheric measurements (e.g., Jiang et al., 2014; Jin et al., 2018;  
 641 Peters et al., 2007). Figure 5 shows the spatial distributions of the mean biases between  
 642 the gaseous pollutants simulated using prior and posterior emissions and assimilated  
 643 observations. In the CEPs, for each species, the distribution of biases was similar to the  
 644 increments in background fields constrained through 3DVAR, as shown in Figure S3.  
 645 For example, almost all sites had large negative biases for CO, while for SO<sub>2</sub> and NO<sub>2</sub>,  
 646 positive biases were mainly distributed over the North China Plain (NCP), Yangtze  
 647 River Delta (YRD), Sichuan Basin (SCB), and Central China and negative biases were  
 648 distributed over remaining areas. After constraining with observations, the biases of all

649 three gaseous air pollutants were significantly reduced at most sites. For CO, the biases  
650 at 62% of the sites decreased to absolute values less than  $0.2 \text{ mg m}^{-3}$  and for SO<sub>2</sub> and  
651 NO<sub>2</sub>, the biases at 52% and 47% of the sites were within  $\pm 4 \text{ } \mu\text{g m}^{-3}$ . However, large  
652 negative biases were still observed in western China, indicating that the uncertainties  
653 of the posterior emissions are still large in western China, which may be attributed to  
654 the large biases in prior emissions and the relatively limited observations. Overall, the  
655 statistics show that there are different levels of improvement at the 311 assimilation  
656 sites of 92%, 85%, and 85% for CO, SO<sub>2</sub>, and NO<sub>2</sub>, respectively. The small number of  
657 sites with worse performance may be related to over-adjusted emissions by EI or  
658 contradictory adjustments caused by opposite biases in adjacent areas.

659 Table 6 lists the statistical results of the evaluations averaged over the whole mainland  
660 of China. For CO, the mean bias was  $-0.8 \text{ mg m}^{-3}$  with the prior emissions, while it  
661 substantially reduced to  $-0.1 \text{ mg m}^{-3}$  (reduction rate of 89.6%) when simulating with  
662 the posterior emissions. Additionally, the RMSE decreased by 48.1% from 1.08 to 0.56  
663  $\text{mg m}^{-3}$ , and the CORR increased by 76.1% from 0.46 to 0.81. For SO<sub>2</sub> and NO<sub>2</sub>, the  
664 regional mean biases slightly increased as the positive/negative biases among different  
665 sites might be offset. However, the RMSEs decreased to 17.7 and 12.3  $\mu\text{g m}^{-3}$ ,  
666 respectively, which were 58.3% and 50.8% lower than those of CEPs, and the CORRs  
667 increased by 125.6% and 35.4%, both reaching up to 0.88, indicating that EI  
668 significantly improved the NO<sub>x</sub> and SO<sub>2</sub> emission estimates.

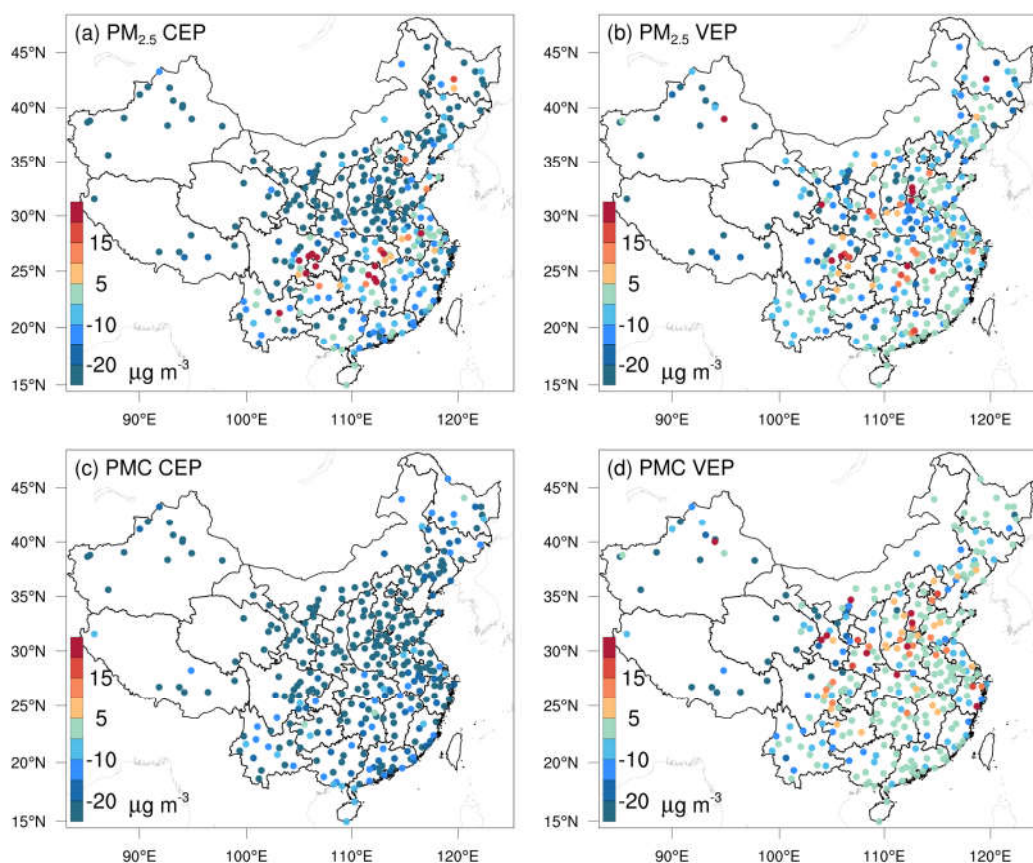


669

670 **Figure 5.** Spatial distribution of the BIAS of the simulated (a, b) CO, (c, d) SO<sub>2</sub>, and  
 671 (e, f) NO<sub>2</sub> with prior (left, CEP) and posterior (right, VEP) emissions. CO unit: mg m<sup>-3</sup>  
 672 <sup>3</sup>; SO<sub>2</sub> and NO<sub>2</sub> units: µg m<sup>-3</sup>.

673 Figure 6 shows the spatial distributions of the mean biases of simulated PM<sub>2.5</sub> and PMC  
 674 evaluated against assimilated observations. Similarly, the CEP simulations did not  
 675 perform well. There were widespread underestimations across the country, with mean  
 676 biases of -24.0 and -32.4 µg m<sup>-3</sup>. After data assimilation, the performance of the VEP  
 677 simulations significantly improved. The biases decreased by 72.1% and 90.4% to -6.7

678 and  $-3.1 \mu\text{g m}^{-3}$ , the RMSEs decreased by 41.2% and 40.7% to 29.6 and  $24.6 \mu\text{g m}^{-3}$ ,  
679 and the CORRs increased by 35.9% and 176.0% to 0.87 and 0.69 for  $\text{PM}_{2.5}$  and PMC,  
680 respectively. Overall, 89.6% and 97.2% of the assimilation sites were improved for  
681  $\text{PM}_{2.5}$  and PMC, respectively. However, compared with the results for the three gaseous  
682 pollutants, there were sites with large biases scattered throughout the entire domain. In  
683 addition to the potential over-adjusted or contradictory adjustments of emissions as in  
684 the three gas species, the sites with large biases may be related to the complex  
685 precursors and complex homogeneous and heterogeneous chemical reactions and  
686 transformation processes of secondary  $\text{PM}_{2.5}$ , and the fact that we did not simulate the  
687 time variation of dust blowing caused by wind speed for PMC owing to the lack of land  
688 cover data that is compatible with the CMAQ dust module and agricultural activity data  
689 to identify dust source regions.

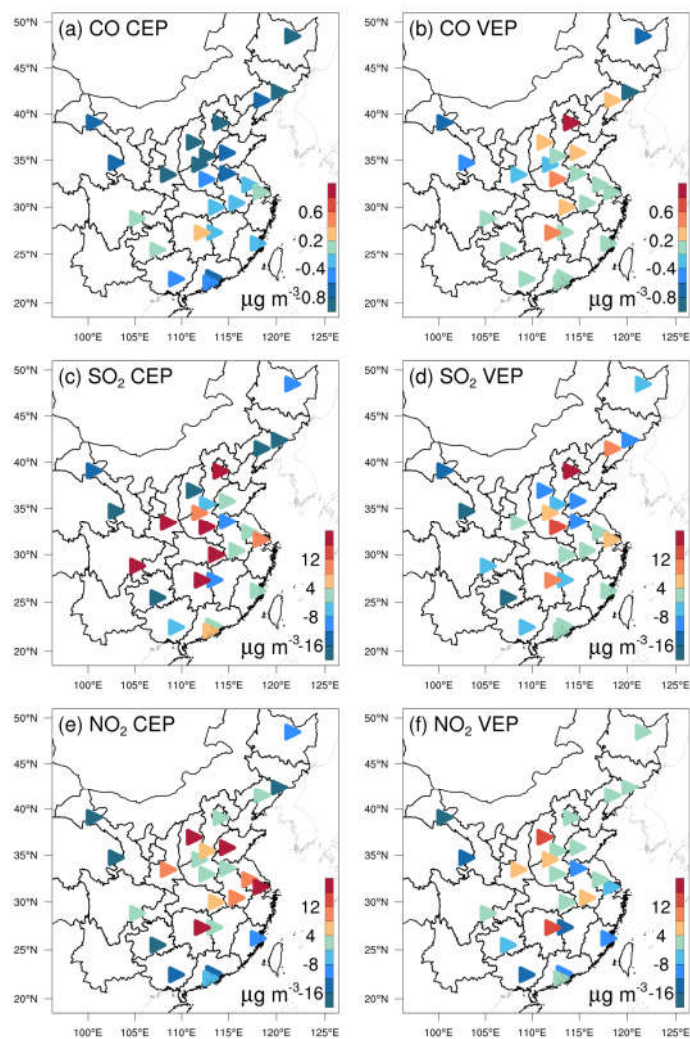


690

691

**Figure 6.** Same as in Figure 5 but for  $\text{PM}_{2.5}$  and PMC.

692 Figures 7 and 8 show the spatial distributions of the biases calculated against  
 693 independent observations for the five species. With posterior emissions, the decreasing  
 694 ratios of RMSEs ranged from 26.7%–42.0% and the CORRs increased by 13.7–59.0%  
 695 to 0.62–0.87. Overall, the biases at the independent sites are similar or slightly worse  
 696 than those at the assimilated sites, which is reasonable as the closer the independent  
 697 sites are to the assimilated site, the more constraints of observation information can be  
 698 obtained and the more significant the improvements in the optimized state variables of  
 699 the model. For example, generally, the transmission distance of NO<sub>2</sub> is relatively short  
 700 and remote cities with small emission correlations to the cities with assimilated  
 701 observations are relatively less constrained, resulting in only a 26.7% decrease in the  
 702 RMSE.

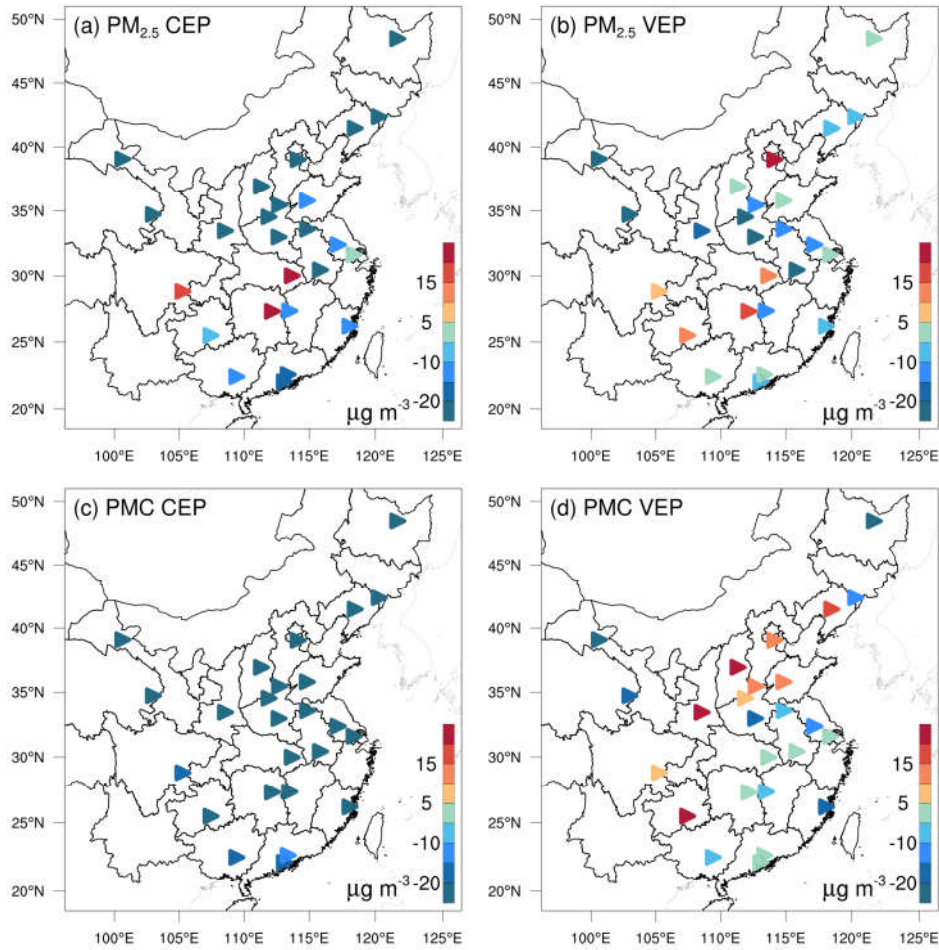


703

704

**Figure 7.** As in Figure 5 but for the independent validation.





705  
706

**Figure 8.** As in Figure 6 but for the independent validation.

707 Comparing our results with those of previous studies, Tang et al. (2013) inverted CO  
708 emissions over Beijing and the surrounding areas and obtained comparable  
709 improvements (Table 6) in the RMSE (37–48% vs. 30–51%) and CORR (both studies  
710 ~ 0.81); however, we decreased the biases by 90–97%, which is much greater than their  
711 48–64% reductions. Additionally, Chen et al. (2019) showed that the RMSE of  
712 simulated SO<sub>2</sub> with updated SO<sub>2</sub> emissions decreased by 4.2–52.2% for different  
713 regions, and the CORR only increased to 0.69 at most. These improvements are smaller  
714 than those obtained in this study, which may be due to the insufficient adjustment of  
715 emissions caused by the underestimated ensemble spread through the inflation method.  
716 The better performance in this study may be related to our inversion process, which  
717 causes the optimized emissions of the current DA window to propagate to the next DA  
718 window for further correction.

719 **Table 6.** Statistics comparing the pollution concentrations from the simulations with  
 720 prior (CEP) and posterior (VEP) emissions against assimilated and independent  
 721 observations, respectively. CO unit: mg m<sup>-3</sup>; others units: µg m<sup>-3</sup>.

Species	Mean Obs.	Mean Sim.		BIAS		RMSE		CORR	
		CEP	VEP	CEP	VEP	CEP	VEP	CEP	VEP
Against assimilated observations									
CO	1.43	0.66	1.36	-0.77	-0.08	1.08	0.56	0.46	0.81
SO <sub>2</sub>	32.5	34.4	28.4	1.9	-4.1	42.4	17.7	0.39	0.88
NO <sub>2</sub>	43.8	40.8	39.0	-2.9	-4.8	25.0	12.3	0.65	0.88
PM <sub>2.5</sub>	77.0	53.1	70.3	-24.0	-6.7	50.3	29.6	0.64	0.87
PMC	40.5	8.1	37.5	-32.4	-3.1	41.5	24.6	0.25	0.69
Against independent observations									
CO	1.54	0.79	1.52	-0.75	-0.02	1.15	0.72	0.59	0.82
SO <sub>2</sub>	40.6	39.2	37.3	-1.3	-3.2	44.3	27.2	0.57	0.87
NO <sub>2</sub>	50.2	50.0	47.5	-0.3	-2.7	21.7	15.9	0.73	0.83
PM <sub>2.5</sub>	91.5	64.6	84.1	-26.9	-7.4	64.1	37.2	0.62	0.87
PMC	42.0	9.2	40.4	-32.8	-1.6	39.3	26.6	0.39	0.62

722 \* BIAS, mean bias; RMSE, root mean square error; CORR, correlation coefficient

#### 723 4.1.4 Uncertainty reduction

724 The uncertainty reduction rate (UR) is an important quantity to evaluate the  
 725 performance of RAPAS and the effectiveness of *in-situ* observations (Chevallier et al.,  
 726 2007; Jiang et al., 2021; Takagi et al., 2011). Following Jiang et al. (2021), the UR was  
 727 calculated as

$$728 \quad UR = \left(1 - \frac{\sigma_{posterior}}{\sigma_{prior}}\right) \times 100 \quad (19)$$

729 where  $\sigma_{posterior}$  and  $\sigma_{prior}$  are the posterior and prior uncertainties, respectively,  
 730 calculated using the standard deviations of the prior and posterior perturbations (Text  
 731 S2). Table 7 shows the URs averaged in each province and mainland China. URs varied  
 732 with species as they are closely related to the magnitude settings of prior uncertainties  
 733 (Jiang et al., 2021). The URs of PPM<sub>2.5</sub> and PMC were the most effective while the UR  
 734 of NO<sub>x</sub> emissions was the lowest. For mainland China overall, uncertainties were  
 735 reduced by 44.4%, 45.0%, 34.3%, 51.8%, and 56.1% for CO, SO<sub>2</sub>, NO<sub>x</sub>, PPM<sub>2.5</sub>, and

736 PMC, respectively. For one species, URs varied across provinces. URs are usually  
 737 related to observation coverage, which means that the more observation constraints  
 738 there are, the more URs decrease. Additionally, URs may also be related to emission  
 739 distributions. Generally, URs were more significant in the provinces where  
 740 observations and emissions were both relatively concentrated (e.g. Tibet), while they  
 741 were much lower where the emissions were scattered or relatively uniform, but the  
 742 observations were only in large cities, even if there were many more observations than  
 743 in other provinces.

744 **Table 7.** Time-averaged posterior emission uncertainty reduction (%) indicated by the  
 745 standard deviation reduction of total emissions per province calculated by prior and  
 746 posterior ensembles.

Province	CO	SO <sub>2</sub>	NO <sub>x</sub>	PPM <sub>2.5</sub>	PMC
Mainland	44.4	45.0	34.3	51.8	56.1
Shanghai	16.9	16.7	20.8	24.7	18.5
Jiangsu	17.7	25.3	29.3	34.1	52.3
Zhejiang	24.7	13.3	17.9	42.4	31.4
Anhui	20.1	52.7	39.1	58.1	40.9
Shandong	32.1	30.0	20.3	53.7	26.7
Beijing	28.2	6.2	37.0	43.3	31.4
Tianjin	20.0	7.0	21.4	41.3	17.8
Hebei	29.5	40.2	28.8	56.0	30.3
Shanxi	38.4	37.9	22.5	55.3	35.0
Neimenggu	30.1	45.8	40.4	37.6	52.8
Henan	27.4	16.1	21.9	53.7	30.8
Hunan	36.0	27.7	34.4	16.9	41.6
Hubei	30.8	16.6	26.0	46.4	46.5
Jiangxi	20.9	28.4	29.4	47.0	46.7
Guangdong	31.2	14.9	41.1	53.1	46.4
Guangxi	22.6	13.9	42.5	48.1	55.2
Fujian	9.9	8.1	31.9	31.6	49.2
Hainan	0.6	0.5	4.5	0.7	23.3
Liaoning	35.6	34.6	19.0	33.9	54.0
Heilongjiang	29.9	27.7	17.4	42.0	65.2
Jilin	27.9	44.5	18.7	42.0	42.8
Shaanxi	41.3	13.2	29.8	47.9	43.1
Gansu	24.8	36.1	33.7	46.3	56.4
Xinjiang	38.3	27.9	20.2	46.3	66.5
Qinghai	53.9	25.8	27.3	46.0	57.9
Ningxia	47.0	36.6	17.6	38.0	30.1
Sichuan	29.4	25.0	39.5	61.1	46.5
Chongqing	5.7	8.2	8.8	12.7	13.8
Guizhou	14.4	16.4	26.6	40.3	38.2
Yunnan	38.3	29.9	31.4	40.1	55.9
Tibet	30.2	0.5	52.8	67.3	73.2

747

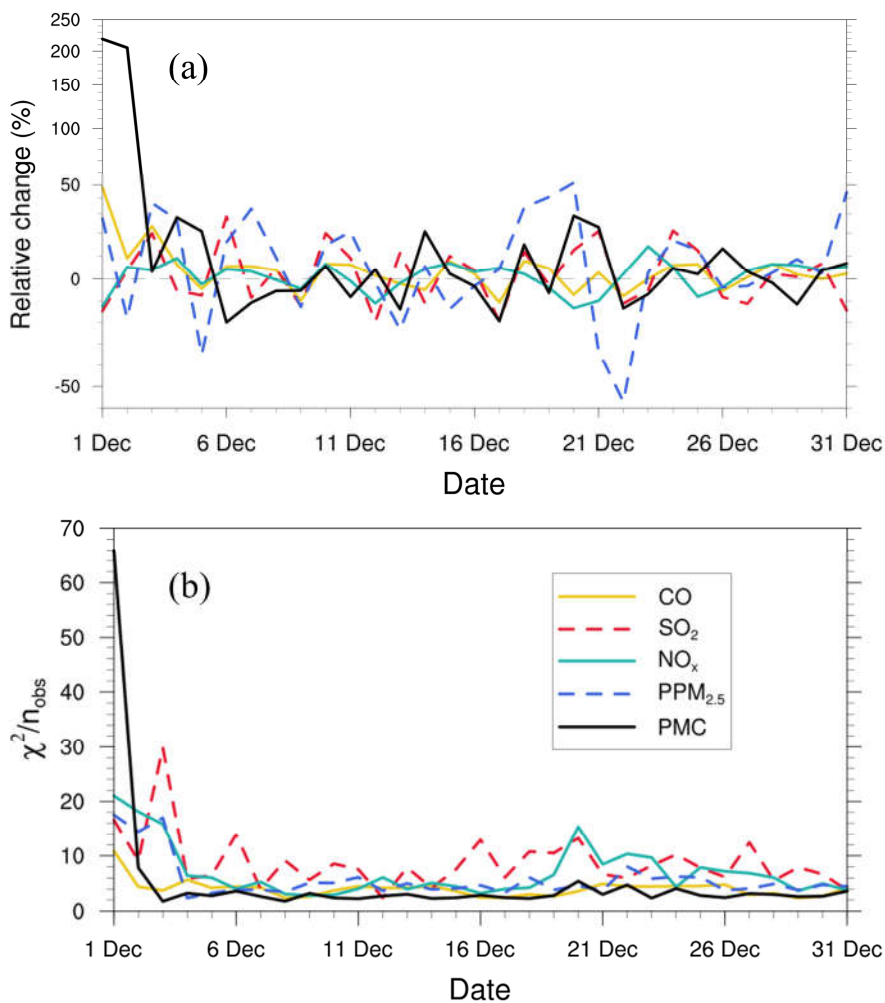
#### 748 4.1.5 Evaluation using chi-squared statistics

749 To diagnose the performance of the EnKF analysis, chi-squared ( $\chi^2$ ) statistics were  
750 calculated, which are generally used to test whether the prior ensemble mean RMSE  
751 with respect to the observations is consistent with the prior “total spread” (square root  
752 of the sum of ensemble variance and observation error variance). Following Zhang et  
753 al. (2015), for the  $t$ -th window,  $\chi^2$  is defined as:

$$754 \quad \chi_t^2 = (\mathbf{y} - \mathbf{H}\overline{\mathbf{X}^b})^T (\mathbf{H}\mathbf{P}^b\mathbf{H}^T + \mathbf{R})^{-1} (\mathbf{y} - \mathbf{H}\overline{\mathbf{X}^b}) \quad (20)$$

755 Figure 9 shows the time series of the relative changes between the prior and posterior  
756 emissions and the  $\chi^2$  statistics. There were relatively large adjustments in emissions in  
757 the first three windows, especially for the PMC. Subsequently, the five species reached  
758 a more optimal state with successive emission inversion cycles. The  $\chi^2$  statistics showed  
759 similar variation characteristics as the daily changes in emissions. The  $\chi^2$  value was  
760 slightly greater than 1, indicating that the uncertainties from the error covariance  
761 statistics did not fully account for the error in the ensemble simulations. A similar result  
762 was reported by Chen et al. (2019). Further investigations should be conducted to  
763 generate larger spreads by accounting for the influence of model errors. As we imposed  
764 the same uncertainty of prior emissions at each DA window to partially compensate for  
765 the influence of model errors,  $\chi^2$  statistics showed small fluctuations, indicating that the  
766 system updated emissions consistently and stably.

767

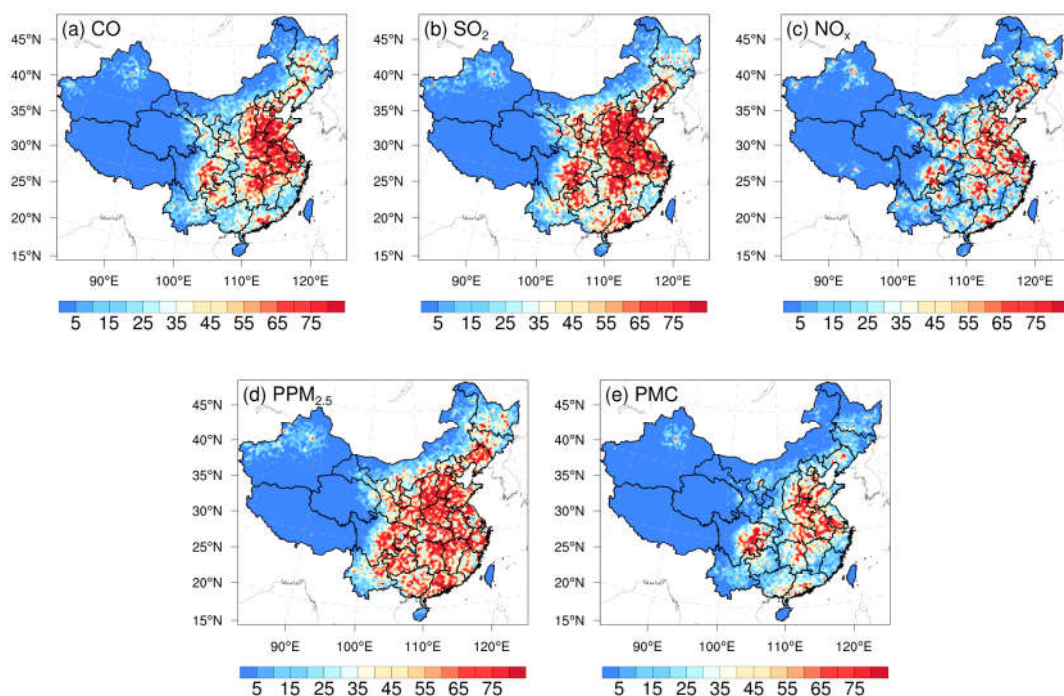


768

769 **Figure 9.** Relative changes (a) in posterior emission estimates of CO, SO<sub>2</sub>, NO<sub>x</sub>, PPM<sub>2.5</sub>,  
 770 and PMC and  $\chi^2$  statistics (b) of these state vectors in each window.

#### 771 4.1.6 Evaluation using OSSE

772 Figure 10 shows the spatial distribution of the error reduction in the posterior emissions  
 773 of the five species. After inversion, in most areas, the emission errors were reduced by  
 774 more than 80%, especially in the central and eastern regions with dense observation  
 775 sites, while in remote areas far away from cities, due to the sparse observation sites, the  
 776 emission errors were still not well adjusted. Overall, the error reduction rates of CO,  
 777 SO<sub>2</sub>, NO<sub>x</sub>, PPM<sub>2.5</sub>, and PMC were 78.4%, 86.1%, 78.8%, 77.6%, and 72.0%,  
 778 respectively, indicating that with the *in-situ* observations in China, RAPAS can  
 779 significantly reduce emission errors and thus showed good performance in emission  
 780 estimates.



781

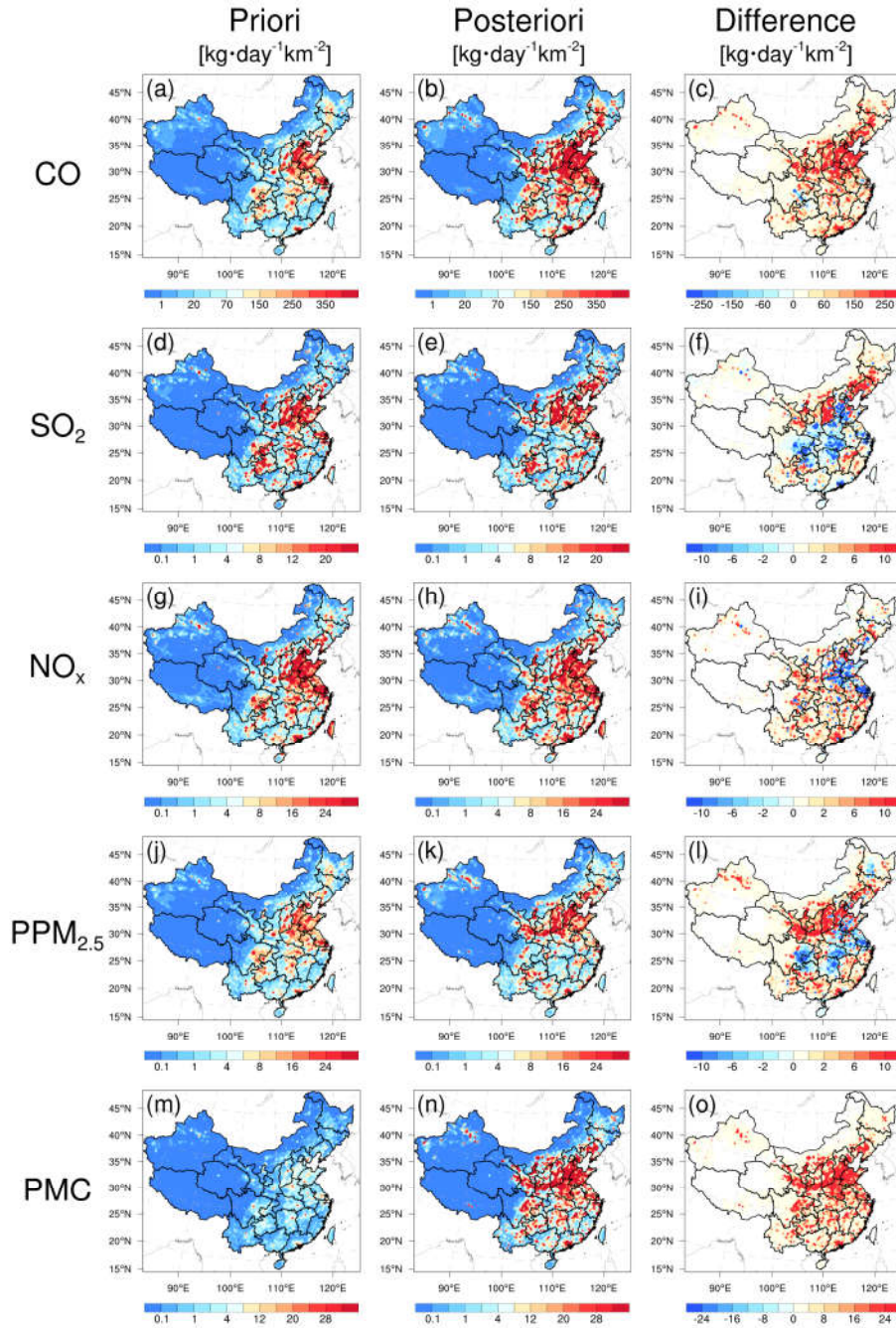
782 **Figure 10.** Spatial distribution of the error reduction (%) of posterior emissions in the  
 783 OSSE.

#### 784 4.2 Inverted emissions

785 Figure 11 shows the spatial distribution of temporally averaged prior and posterior  
 786 emissions and their differences in emissions in December 2016. It should be noted that  
 787 emissions outside China were masked; as the observation sites were limited to China in  
 788 this study, there was a slight change in the emissions outside China. Higher emissions  
 789 were mainly concentrated in central and eastern China, especially in the NCP, YRD,  
 790 and Pearl River Delta~~PRD~~, and lower emissions occurred across Northwest and  
 791 Southern China. Compared with the prior emissions, posterior CO emissions were  
 792 considerably increased across most areas of mainland China, especially in northern  
 793 China, with an overall increase of 129%. A notable underestimation of prior emissions  
 794 was also confirmed by inversion estimations (Feng et al., 2020b; Tang et al., 2013; Wu  
 795 et al., 2020) and model evaluations (Kong et al., 2019b) in previous studies. For SO<sub>2</sub>,  
 796 the emissions increased mainly in Northeast China, Shanxi, Ningxia, Gansu, Fujian,  
 797 Jiangxi, and Yunnan provinces. In SCB, Central China, YRD, and part of the NCP,

798 emissions were significantly reduced. The national total SO<sub>2</sub> emissions increased by  
799 20%. For NO<sub>x</sub>, although the increment of national total emissions was small  
800 (approximately 5%), there were large deviations. The emissions in NCP and YRD were  
801 reduced, whereas the emissions in most cities in other regions increased. The changes  
802 in the emission of PPM<sub>2.5</sub> were similar to those of SO<sub>2</sub>. Compared with the prior  
803 emissions, the posterior PPM<sub>2.5</sub> emissions decreased over central China, SCB, and YRD,  
804 whereas those in southern and northern China increased, especially in Shanxi, Shaanxi,  
805 Gansu, and southern Hebei provinces. Overall, the relative increase was 95%. For PMC,  
806 the posterior emissions were increased over all of mainland China, with a national mean  
807 relative increase ~~exceeding of 1000~~1045%. Larger emission increments mainly  
808 occurred in areas with significant anthropogenic emissions of CO and PPM<sub>2.5</sub>,  
809 indicating that the large underestimation of PMC emissions in the prior inventory may  
810 be mainly attributed to the underestimations of anthropogenic activities. The absence  
811 of natural dust is another reason, as the wind-blown dust scheme was not applied in this  
812 study. Overall, PM<sub>10</sub> emissions (PPM<sub>2.5</sub>+PMC) increased by 318%. If we assume that  
813 all the increments in PM<sub>10</sub> emissions are from natural dust, that means the contribution  
814 of natural dust accounted for 75% of total PM<sub>10</sub> emissions, which is consistent with the  
815 source apportionment of PM<sub>10</sub> of 75% in Changsha in Central China (Li et al., 2010).  
816 Large PMC emission increments were also reported by Ma et al. (2019).

817 Detailed estimations of posterior emissions and relative changes compared to prior  
818 emissions in each province and mainland China are given in Table S1. The evaluation  
819 results for July showed that the emission uncertainty could still be significantly reduced  
820 and the performance of the system in July was comparable to that in December (Table  
821 S2). Additionally, the seasonal variation in emissions was well reflected (Figures S4  
822 and S5), which means that our system performed well at different times of the year.  
823 Note that the differences, excluding PMC, between the prior and posterior emissions  
824 mainly reflect the deficiencies of the prior emissions as the times of the prior emissions  
825 and observations were consistent in this study.



826

827 **Figure 11.** Spatial distribution of the time-averaged prior emissions (left column, MEIC  
 828 2016), posterior emissions (middle column), and differences (right column, posterior  
 829 minus prior).

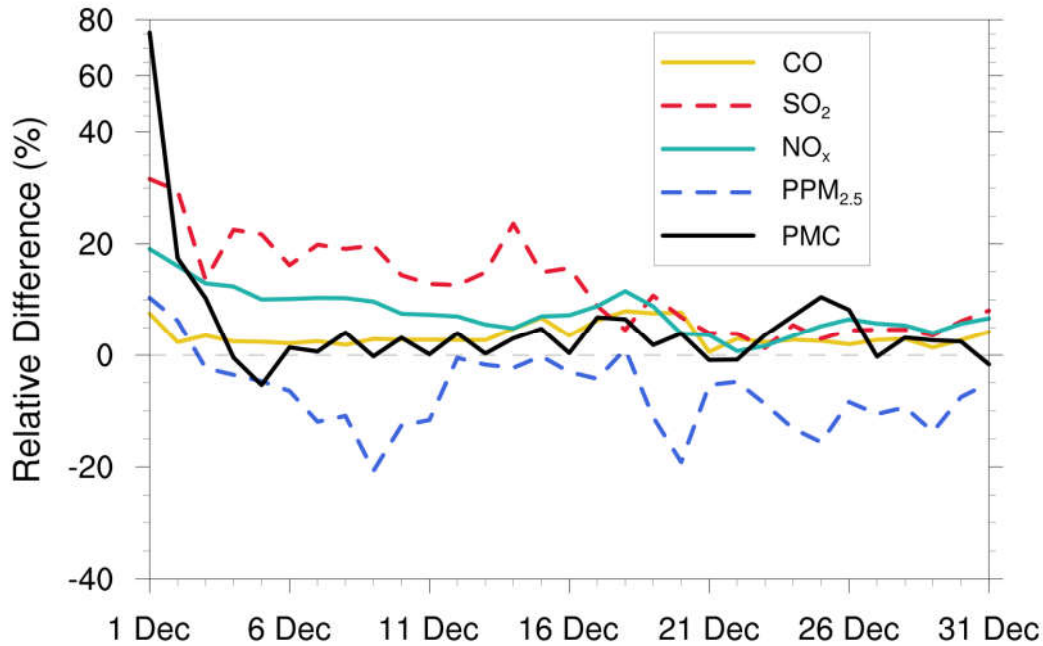
### 830 4.3 Sensitivity tests

#### 831 4.3.1 Impact of prior inventories

832 Various prior inventories have shown considerable differences in space allocation and



833 emission magnitudes. Inversion results can be sensitive to a priori emissions if the  
834 observations are insufficient (Gurney et al., 2004; He et al., 2018). MEIC 2012 was  
835 used as an alternative a priori in EMS1 to investigate the impact of different prior  
836 emissions on posterior emissions. Figure 12 shows the time series of the relative  
837 differences in the daily posterior emissions of the five species between the EMDA (base)  
838 and EMS1 experiments. Overall, the differences between the two posterior emissions  
839 gradually decreased over time. At the beginning, the differences in the CO, SO<sub>2</sub>, NO<sub>x</sub>,  
840 PPM<sub>2.5</sub>, and PMC between the two inventories (i.e. MEIC 2012 vs. MEIC 2016) were  
841 17.5%, 114.5%, 30.8%, 46.0%, and 72.0%, respectively, compared to 2.5%, 4.5%,  
842 4.5%, -8.9%, and 3.0% in the last ten days. In addition, the species with larger emission  
843 differences at the beginning took a longer time (i.e. more DA steps) to achieve  
844 convergence. The quick convergence of PMC emissions was attributed to the large prior  
845 uncertainty of 100% used in the first three DA windows. In contrast to the other species,  
846 there were significant negative deviations in PPM<sub>2.5</sub> emissions between the two  
847 experiments. This may be due to the positive deviations in the precursors of PM<sub>2.5</sub> (i.e.,  
848 SO<sub>2</sub> and NO<sub>x</sub>), which lead to a larger amount of secondary production. The PPM<sub>2.5</sub>  
849 emissions will be reduced to balance the total PM<sub>2.5</sub>. We compared the PM<sub>2.5</sub>  
850 concentrations simulated by the two optimized inventories and found that they were  
851 almost the same (Figure S6). Overall, this indicates that observations in China were  
852 sufficient to infer emissions and that our system was robust. Meanwhile, the monthly  
853 posterior emissions shown in Section 4.2 were still underestimated to a certain extent.



854

855 **Figure 12.** Relative differences in CO, SO<sub>2</sub>, NO<sub>x</sub>, PPM<sub>2.5</sub>, and PMC emissions (% the  
 856 ratio of absolute difference to EMDA) between the EMDA and EMS1 experiments.

857

#### 858 **4.3.2 Impact of prior uncertainties settings**

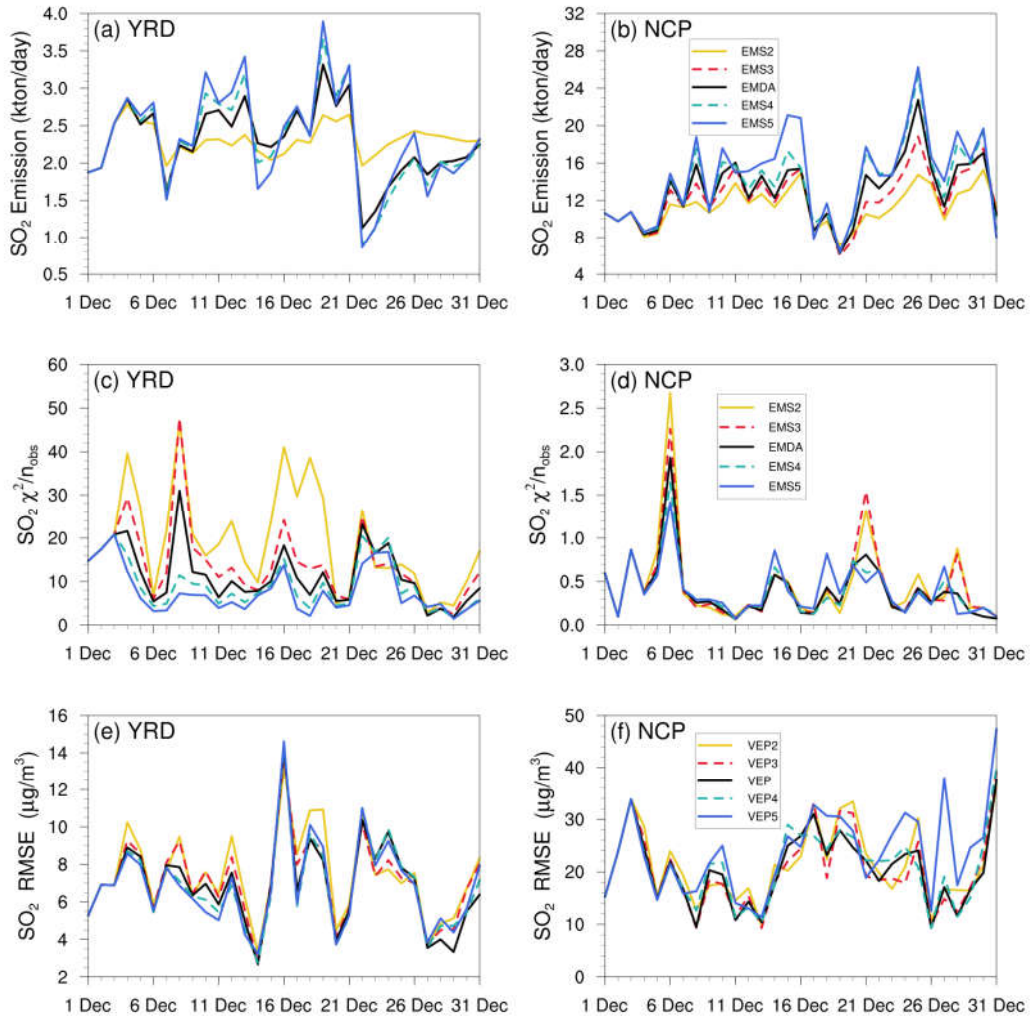
859 The uncertainty of prior emissions determines how closely the analysis is weighted  
 860 towards the background and observations; however, information about prior  
 861 uncertainties is generally not readily available. To evaluate the possible influence of  
 862 prior uncertainties on the optimized emissions, we increased/reduced the uncertainties  
 863 after three days of cycling, namely starting at 0000 UTC, 3 December, by 25% and 50 %  
 864 in EMS2 (-50%), EMS3 (-25%), EMS4 (+25%), and EMS5 (+50%), respectively. Table  
 865 8 summarizes the emission changes with different prior uncertainty settings in the  
 866 EMS2–5 experiments. To better understand the response of the system to the emission  
 867 uncertainty settings, Figure 13 illustrates the time series of SO<sub>2</sub> emission changes, Chi-  
 868 square statistics, and RMSEs of simulated SO<sub>2</sub> with emissions updated in the EMDA  
 869 and EMS2–5 experiments over the YRD and NCP (Figure 2). Compared with the  
 870 EMDA, when the uncertainties decreased (increased), the emissions of the five species  
 871 decreased (increased) accordingly. This is because the posterior emissions of the five  
 872 species were larger than the prior emissions and, as shown in Figure 13a–d, larger

873 uncertainty will lead to faster convergence, resulting in larger posterior emissions. It  
874 can also be seen from Figure 13 that a faster convergence will reduce the RMSE of the  
875 simulated concentration with the posterior emissions in the early stage of the  
876 experiment; however, in the later stage of the experiment, there were no significant  
877 differences in the RMSE and Chi-square statistics among the different experiments.  
878 However, day-to-day changes in emissions also cause slight fluctuations. In addition,  
879 when greater uncertainties are set, the day-to-day changes in emissions are more drastic,  
880 resulting in a larger RMSE, as shown in the NCP. Moreover, the significant day-to-day  
881 variations in the estimated emissions may not be in line with the actual situation. Owing  
882 to the spatial-temporal inhomogeneity of emissions, the differences in Chi-square  
883 statistics between the YRD and NCP show that it may be necessary to apply different a  
884 priori uncertainties according to different regions (Chen et al., 2019). Therefore, when  
885 using an EnKF system for emission estimation, error setting must be carefully executed.  
886 Overall, the uncertainties chosen in EMDA aim to minimize the deviation of the  
887 concentration fields and maintain the stability of the inversion.

888 **Table 8.** Relative differences in CO, SO<sub>2</sub>, NO<sub>x</sub>, PPM<sub>2.5</sub> and PMC emissions (% , the  
889 ratio of absolute difference to EMDA) between the EMDA and EMS2-5 experiments.

Species	EMS2	EMS3	EMS4	EMS5
CO	-8.6	-4	3	5.2
SO <sub>2</sub>	-14	-5.7	3.6	6.8
NO <sub>x</sub>	-6.5	-3	2.8	4.5
PPM <sub>2.5</sub>	-16.5	-7.8	4.6	8.7
PMC	-18.5	-8.2	7.3	13.1

890



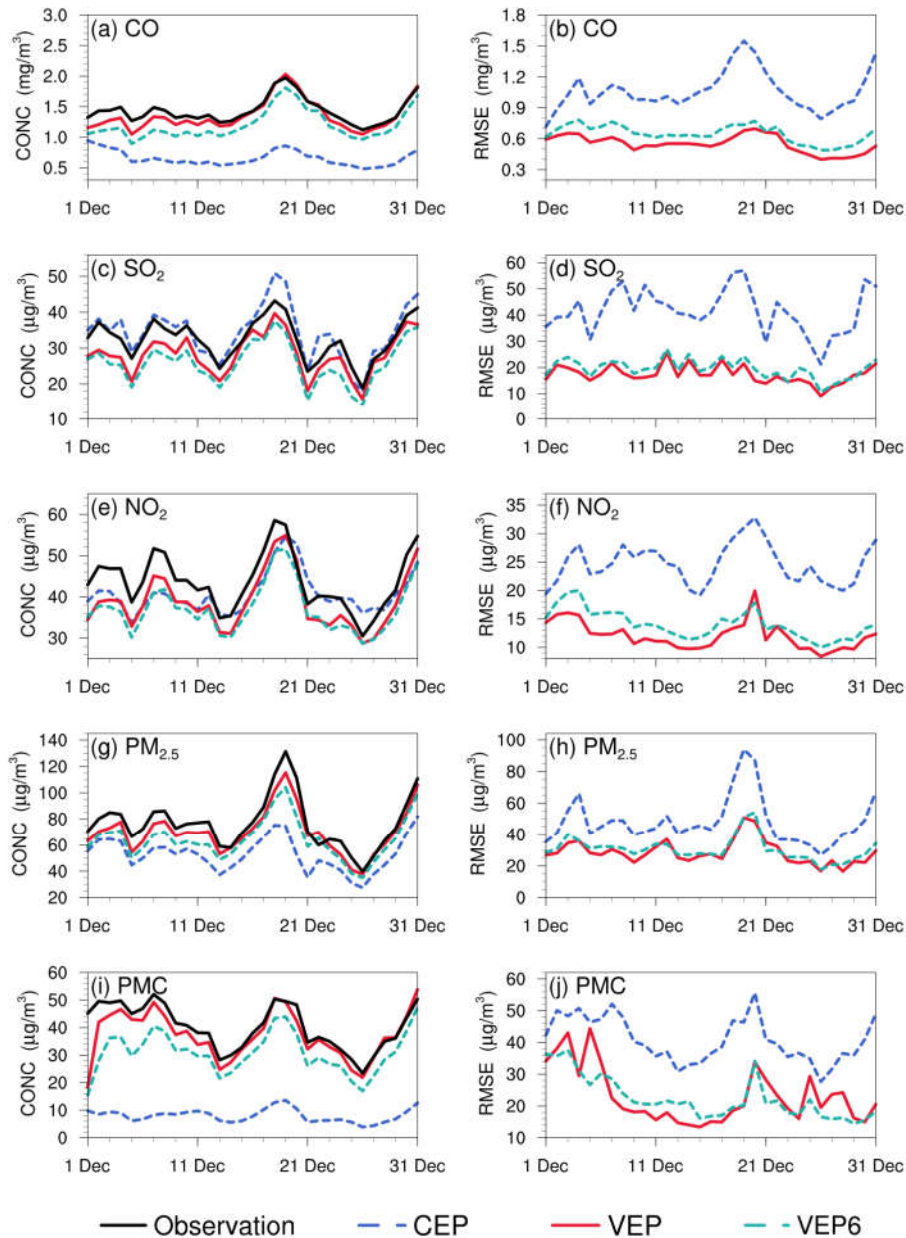
891

892 **Figure 13.** Time-series of SO<sub>2</sub> emission changes, Chi-square statistics, and RMSE of  
 893 simulated SO<sub>2</sub> with updated SO<sub>2</sub> emissions in the EMDA and EMS2-5 experiments  
 894 over the YRD and NCP.

### 895 4.3.3 Impact of observation error settings

896 Observation errors are another factor that determine the relative weights of the  
 897 observations and background in the analysis. A proper estimate of the observation error  
 898 is important for filter performance; however, observation errors are generally not  
 899 provided with datasets. The observation error is usually set to a fixed value (Ma et al.,  
 900 2019), specific proportion of the observation value (Tang et al., 2013), or value  
 901 calculated by combining measurement error with representative error as used in this  
 902 study. Generally, the performance of data assimilation is sensitive to the specification

903 of the observation error (Tang et al., 2013). AsSensitivity experiment (EMS6) with  
904 doubled observation error was conducted to evaluate the influence of observation error  
905 on the optimized emissions. Overall, the spatial distribution of emissions after  
906 optimization was almost the same as that of the EMDA experiment but with a lower  
907 increment (Figure S7), resulting in a weaker estimate of the national total emissions for  
908 each species. This is because that the observation error inflates and the system becomes  
909 more certain of the prior emission, and reduces the effect of observation information.  
910 Figure 14 shows the time series of simulated and observed daily concentrations and  
911 their RMSEs verified against the assimilated sites. The simulations in VEP6 usually  
912 performed worse, with larger biases and RMSEs than those of VEP (Figures S8 and S9),  
913 especially in western and southern China, where posterior emissions were significantly  
914 underestimated. These results generally corresponded to sluggish emission changes and  
915 large Chi-square statistics (Figure S10), suggesting that an observation error that is too  
916 large may substantially impact the estimated emissions.



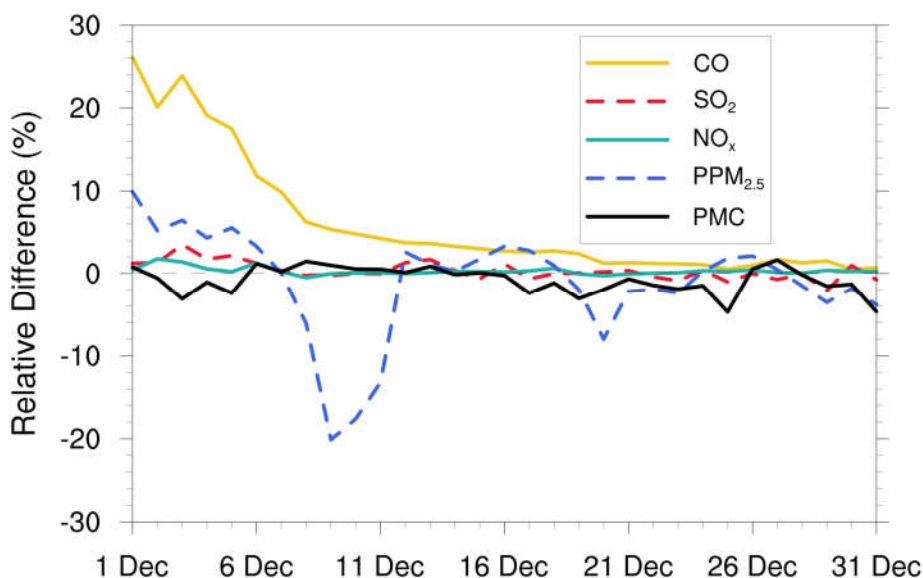
917

918 **Figure 14.** Time series of the daily concentrations (CONC, left) and root mean square  
 919 error (RMSE, right) obtained from CEP, VEP, and VEP<sub>67</sub>. The simulations were  
 920 verified against the assimilated sites.

#### 921 4.3.4 Impact of the IC optimization of the first window

922 Several studies indicate large emission discrepancies resulting from IC errors (Jiang et  
 923 al., 2013a; Miyazaki et al., 2017; Tang et al., 2013), which means that if the IC is not  
 924 optimized, the errors of concentrations would be compensated for through the  
 925 adjustment of emissions. To evaluate the impact of IC optimization of the first window

926 on the emission inversions, an EMS7 experiment without the IA step was conducted.  
 927 Figure 15 shows the time series of the relative differences in the daily posterior  
 928 emissions of the five species between the EMDA and EMS7 experiments. It can be  
 929 observed that IC optimization had a significant impact on the emission inversions of  
 930 long-lived species (i.e. CO). The overall difference in the inverted CO emissions  
 931 between the two experiments was approximately 5.3% but can reach 26.1% in the first  
 932 few windows. For the short-lived species, IC optimization had little impact on the  
 933 emissions; for example, the average emission differences of SO<sub>2</sub>, NO<sub>x</sub>, and PMC in the  
 934 two experiments were 0.3%, 0.3%, and 0.9%, respectively. For PPM<sub>2.5</sub>, the average  
 935 emission difference is affected not only by primary emissions, but also by the complex  
 936 chemistry of its precursors. Therefore, the difference between the two experiments  
 937 fluctuated, with overall difference of 2%. Notably, with the gradual disappearance of  
 938 the benefit of IC assimilation, the two experiments reached a unified state after several  
 939 windows. For CO, the impact of IA on emission inversion lasted approximately half a  
 940 month. These results indicate that removing the bias of the IC of the first DA window  
 941 is essential for the subsequent inverse analysis (Jiang et al., 2017).



942

943 **Figure 15.** Relative differences in CO, SO<sub>2</sub>, NO<sub>x</sub>, PPM<sub>2.5</sub>, and PMC emissions (% the  
 944 ratio of absolute difference to EMDA) between the EMDA and EMS7.

#### 945 **4.4 Discussion**

946 Optimal state estimation using an EnKF relies on the assumption of an unbiased  
947 Gaussian prior error, which is not guaranteed in such highly nonlinear and large bias  
948 systems. In this study, some pollutants (e.g. CO, PMC) have very large simulated biases;  
949 thus, if a small uncertainty is adopted, the emission bias cannot be fully reduced. If a  
950 very large uncertainty is adopted, then the degree of freedom of adjustment is too large  
951 and the inverted daily emissions will fluctuate abnormally. Therefore, we only set a  
952 larger prior uncertainty in the first three windows, adopting a moderate uncertainty in  
953 the following windows and used a “two-step” inversion scheme and cyclic iteration to  
954 gradually correct the emission errors. Figure 9a shows the time series of the relative  
955 differences between prior and posterior emissions in each window. There were  
956 relatively large adjustments for the emissions in the first three windows, especially for  
957 PMC, but the adjustment ranges of the five species after the first three windows were  
958 within the uncertainty range (e.g.  $\pm 25\%$ ), indicating that with this scheme, the EnKF  
959 method used in this system had a good performance in emission inversion.

960 Model-data mismatch errors are from both the emissions and the inherent model errors  
961 arising from the model structure, discretization, parameterizations, and biases in the  
962 simulated meteorological fields. Neglecting model errors would attribute all  
963 uncertainties to emissions and lead to considerable bias in the estimated emissions. In  
964 the version of the CMAQ model used in this study, there are no heterogeneous reactions  
965 (Quan et al., 2015; Wang et al., 2017), the parameterization scheme for the formation  
966 of secondary organic aerosols (SOA) is imperfect (Carlton et al., 2008; Jiang et al.,  
967 2012; Yang et al., 2019), no feedback between chemistry and meteorology was  
968 considered, and we used an idea profile for chemical lateral boundary conditions. All  
969 the above problems can lead to underestimated concentrations of pollutants, which in  
970 turn require more emissions to compensate, leading to overestimation of emissions. In  
971 addition, previous studies showed that ammonia emissions in the MEIC inventory are  
972 underestimated (Kong et al., 2019b; Paulot et al., 2014; Zhang et al., 2018). Owing to  
973 lack of ammonia observations, our system does not include emission estimates of



974 ammonia, which means that the concentration of ammonium aerosol was  
975 underestimated in this system, also resulting in an overestimation of the  $\text{PPM}_{2.5}$   
976 emission. Wind-blown dust was also not simulated; thus, the PMC emission inverted in  
977 this system come from anthropogenic activities and natural sources. Although some of  
978 these shortcomings can be solved by updating the CTM model, there will still be errors  
979 in each parameterization and process. In general, a parameter estimation method was  
980 used to reduce the model errors, in which some uncertain parameters were included in  
981 the augmented state vector and optimized synchronously based on the available  
982 observations (Brandhorst et al., 2017; Evensen, 2009). However, it is difficult to  
983 identify the key uncertain parameters of different species in different models, which  
984 generally comes not only from the complex atmospheric chemical model but also from  
985 hundreds of model inputs (Tang et al., 2013). Another method is bias correction, which  
986 treats the model error as a bias term and includes it in an augmented state vector  
987 (Brandhorst et al., 2017; De Lannoy et al., 2007; Keppenne et al., 2005). In addition,  
988 the weak-constraint 4DVAR method can be used to reduce model errors, which adds a  
989 correction term in the model integration to account for the different sources of model  
990 error (Sasaki, 1970). Although the reliable diagnosis of model error remains a challenge  
991 (Laloyaux et al., 2020), it should be considered in an assimilation system. In the future,  
992 we will consider model errors in our system to obtain better emission estimates.

993 Independent variable localization was adopted to avoid potential spurious correlations  
994 across different species in this study. However, the transmission scales for different  
995 species in different regions differ, and a more accurate localization range can be  
996 obtained through backward trajectory analysis. In addition,  $\text{O}_3$  observations were not  
997 assimilated to improve  $\text{NO}_x$  and VOC emissions using cross-species information.  $\text{O}_3$   
998 concentration and  $\text{NO}_x$  (VOC) emissions were positively correlated in the  $\text{NO}_x$  (VOC)-  
999 limited region and negatively correlated in the VOC ( $\text{NO}_x$ )-limited region (Tang et al.,  
1000 2011; Wang et al., 2019b). Hamer et al. (2015) successfully used  $\text{O}_3$  observations to  
1001 estimate  $\text{NO}_x$  and VOC emissions within the 4DVAR framework within an ideal model.  
1002 However, the  $\text{NO}_x$  emissions are often point or line sources, which are all small

1003 compared to the model resolution. With a coarse spatial resolution, the model cannot  
1004 accurately simulate the relationships between O<sub>3</sub> and its precursors. When assimilating  
1005 O<sub>3</sub> observations to infer NO<sub>x</sub> or VOC emissions, the inaccurate relationships simulated  
1006 by model would worsen the inversion of NO<sub>x</sub> emissions (Inness et al., 2015). In general,  
1007 improving the model resolution can improve the detailed simulation and provide better  
1008 prior information on O<sub>3</sub>-NO<sub>x</sub>-VOC, but it is still difficult to determine whether the  
1009 condition is NO<sub>x</sub>-limited or VOC-limited in the real atmosphere using prior emissions  
1010 (Liu and Shi, 2021). Elbern et al. (2007) emphasized that assimilating O<sub>3</sub> to correct NO<sub>x</sub>  
1011 or VOC emissions must follow the EKMA framework derived based on observations,  
1012 otherwise, even if the resolution is improved to sufficiently solve point and line sources,  
1013 precursor emissions may be still adjusted in an opposite direction. This can be  
1014 demonstrated in our OSSE experiment at high resolution of 3 km (Figure S11). In this  
1015 study, the spatial resolutions of the prior emission inventory (i.e., MEIC) is 0.25° ×  
1016 0.25°, which is appropriate for modeling at regional scales (Zheng et al., 2017). With  
1017 this emission inventory, it is unable to accurately simulate the O<sub>3</sub>-NO<sub>x</sub>-VOC  
1018 relationships. Therefore, to avoid the impact of inaccurate O<sub>3</sub>-NO<sub>x</sub> relationship on  
1019 emission inversion, in our system, we did not assimilate O<sub>3</sub>, but directly assimilate NO<sub>2</sub>  
1020 to optimize the NO<sub>x</sub> emissions. This work will be followed by an ongoing study using  
1021 the available VOC observations.

1022 Although we do not assimilate O<sub>3</sub> observation, model resolution still has some influence  
1023 on inversion results. In our previous study (Feng et al., 2022), we have inferred the NO<sub>x</sub>  
1024 emissions over YRD in China using NO<sub>2</sub> observations, which has a spatial resolution  
1025 of 12 km. The study period, assimilated observations, and inversion settings are the  
1026 same as this study. We compared the posterior emissions of YRD between this study  
1027 and Feng et al. (2022). The results showed that there was similar spatial distribution of  
1028 posterior emissions inferred using the two resolutions (36 km vs 12 km) (Figure S12),  
1029 but the total NO<sub>x</sub> emission in YRD inferred using 36 km resolution was about 8.8%  
1030 higher than that inferred using 12 km resolution. The differences are mainly caused by  
1031 meteorological differences at different resolutions. This indicates that coarse model

1032 resolution may lead to some overestimation of the inverted emissions. In addition, as  
1033 shown previously, the concentrations after DA were evidently underestimated in  
1034 western China, indicating that the inverted emissions over these regions still have large  
1035 uncertainties because of the sparsity of observations, which are spatially insufficient for  
1036 sampling the inhomogeneity of emissions. Therefore, further investigations with the  
1037 joint assimilation of multisource observations (e.g. satellite) are underway.

1038 NO<sub>x</sub> is mainly emitted by transportation (Li et al., 2017), which can reflect the level of  
1039 economic activity to a certain extent. Weekly emission changes were explored to verify  
1040 the performance of the system in depicting emission changes (Figure S13). Although  
1041 the “weekend effect” of emissions in China is not significant (Wang et al., 2014; Wang  
1042 et al., 2015), the posterior NO<sub>x</sub> emission changes are in good agreement with the  
1043 observations. In our previous studies (Feng et al., 2020a; Feng et al., 2020b), this system  
1044 was successfully applied to optimize NO<sub>x</sub> and CO emissions. The inverted emission  
1045 changes were also in line with the epidemic control time points. Additionally, the  
1046 emission changes can reflect the emission migration from developed or urban areas to  
1047 developing or surrounding areas in recent years, which is consistent with the emission  
1048 control strategies in China. Although the system did not consider the model error,  
1049 resulting in a certain difference between the posterior and actual emissions, the  
1050 spatiotemporal changes in posterior emissions were relatively reasonable and can be  
1051 used to monitor emission changes and inform emission regulations.

## 1052 **5 Summary and conclusions**

1053 In this study, we developed a Regional multi-Air Pollutant Assimilation System  
1054 (RAPASv1.0) based on the WRF/CMAQ model, 3DVAR algorithm, and EnKF  
1055 algorithm. RAPAS can quantitatively optimize gridded emissions of CO, SO<sub>2</sub>, NO<sub>x</sub>,  
1056 PPM<sub>2.5</sub>, and PMC on a regional scale by simultaneously assimilating hourly *in-situ*  
1057 measurements of CO, SO<sub>2</sub>, NO<sub>2</sub>, PM<sub>2.5</sub>, and PM<sub>10</sub>. This system includes two subsystems:  
1058 IA subsystem and EI subsystem, which optimize chemical ICs and infer anthropogenic  
1059 emissions.

1060 Taking the 2016 MEIC in December as a priori, the emissions of CO, SO<sub>2</sub>, NO<sub>x</sub>, PPM<sub>2.5</sub>,  
1061 and PMC in December 2016 were inferred by assimilating the corresponding  
1062 nationwide observations over China. The optimized ICs and posterior emissions were  
1063 examined against assimilated and independent observations through parallel forward  
1064 simulation experiments with and without DA. Sensitivity tests were performed to  
1065 investigate the impact of different inversion processes, prior emissions, prior  
1066 uncertainties, and observation errors on emission estimates.

1067 RAPAS showed a good performance in assimilating surface *in-situ* observations, with  
1068 the calculated emission uncertainties reduced by 44.4%, 45.0%, 34.3%, 51.8%, and  
1069 56.1% for CO, SO<sub>2</sub>, NO<sub>x</sub>, PPM<sub>2.5</sub>, and PMC, respectively. It can also significantly  
1070 improve the simulations; the RMSEs of the simulated concentrations with posterior  
1071 emissions decreased by 40.1–56.3% and the CORRs increased from 0.26–0.66 to 0.69–  
1072 0.87 for different species. The OSSE experiment showed that the errors of posterior CO,  
1073 SO<sub>2</sub>, NO<sub>x</sub>, PPM<sub>2.5</sub>, and PMC could be reduced by 78.4%, 86.1%, 78.8%, 77.6%, and  
1074 72.0%, respectively. Overall, compared with the prior emissions (MEIC 2016), the  
1075 posterior emissions increased by 129%, 20%, 5%, and 95% for CO, SO<sub>2</sub>, NO<sub>x</sub>, and  
1076 PPM<sub>2.5</sub>, respectively. The posterior PMC emissions, which included anthropogenic and  
1077 natural dust contributions, increased by 1045%. Sensitivity tests with different prior  
1078 inventories showed that the observations in China were sufficient to infer emission and  
1079 that our system was less dependent on prior inventories. Additionally, sensitivity tests  
1080 with different prior uncertainties indicated that when the posterior emissions were  
1081 larger than the prior emissions, the emissions decreased/increased with  
1082 decreases/increases in uncertainties because of the different convergence rates. These  
1083 results demonstrate the advantage of the two-step method in emission inversion in that  
1084 the inversion errors of the last window can be transferred to the current window for  
1085 further optimization and robustness of the emissions estimated from RAPAS using  
1086 nationwide observations over China. It should be noted that the system usually responds  
1087 slowly to too small a priori uncertainties or too large observation errors, which may  
1088 result in large errors in the estimated emissions.

1089 In summary, the comprehensive evaluation and sensitivity tests revealed that RAPAS  
1090 could serve as a useful tool for accurately quantifying the spatial and temporal changes  
1091 in multi-species emissions at regional scales and near-real time, which will be helpful  
1092 for air pollution control in China and other regions around the world with dense ground  
1093 observation networks.

1094

### 1095 **Code and data availability**

1096 The codes of RAPAS v1.0 are available at <https://doi.org/10.5281/zenodo.5566225>.  
1097 The WRF model code is open-source code and can be obtained from the WRF Model  
1098 User's Page (<https://www2.mmm.ucar.edu/wrf/users>, last access: 25 April 2021). The  
1099 CMAQ model is available through an open license as well (<https://www.epa.gov/cmaq>,  
1100 last access: 25 April 2021). The observational and emission data used in this study are  
1101 available at <https://doi.org/10.5281/zenodo.4718290> (Feng and Jiang, 2021).

1102

### 1103 **Author contribution**

1104 SF, FJ, ZW and ZJ developed RAPAS v1.0. SF and FJ designed the research. SF  
1105 performed model simulations, analyzed data, and prepared the paper with contributions  
1106 from all co-authors. FJ supervised the model development project and assisted in  
1107 conceptualization and writing. HW, WH, YS, LZ, YZ, CL, and WJ contributed to the  
1108 discussion and improvement of the paper.

1109

### 1110 **Competing interests**

1111 The authors declare that they have no conflict of interest.

1112

1113

## 1114 **Acknowledgements**

1115 This work is supported by the National Key R&D Program of China (Grant No.  
1116 2020YFA0607504), the National Natural Science Foundation of China (Grant No.  
1117 41907378), and the Nanjing University Innovation and Creative Program for Ph.D.  
1118 candidate (Grant No. CXCY19-60). We are grateful to the High Performance  
1119 Computing Center (HPCC) of Nanjing University for doing the numerical calculations  
1120 in this paper on its blade cluster system, and thank the MEIC team for providing the  
1121 prior anthropogenic emissions (<http://www.meicmodel.org/>).

1122

## 1123 **References**

1124 Appel, K. W., Pouliot, G. A., Simon, H., Sarwar, G., Pye, H. O. T., Napelenok, S. L., Akhtar, F., and  
1125 Roselle, S. J.: Evaluation of dust and trace metal estimates from the Community Multiscale Air  
1126 Quality (CMAQ) model version 5.0, *Geoscientific Model Development*, 6, 883-899,  
1127 10.5194/gmd-6-883-2013, 2013.

1128 Alexe, M., Bergamaschi, P., Segers, A., Detmers, R., Butz, A., Hasekamp, O., Guerlet, S., Parker,  
1129 R., Boesch, H., Frankenberg, C., Scheepmaker, R. A., Dlugokencky, E., Sweeney, C., Wofsy,  
1130 S. C., and Kort, E. A.: Inverse modelling of CH<sub>4</sub> emissions for 2010-2011 using different  
1131 satellite retrieval products from GOSAT and SCIAMACHY, *Atmospheric Chemistry and  
1132 Physics*, 15, 113-133, 2015.

1133 Barbu, A. L., Segers, A. J., Schaap, M., Heemink, A. W., and Builtjes, P. J. H.: A multi-component  
1134 data assimilation experiment directed to sulphur dioxide and sulphate over Europe,  
1135 *Atmospheric Environment*, 43, 1622-1631, 2009.

1136 Bocquet, M.: Parameter-field estimation for atmospheric dispersion: application to the Chernobyl  
1137 accident using 4D-Var, *Quarterly Journal of the Royal Meteorological Society*, 138, 664-681,  
1138 2012.

1139 Bocquet, M., Elbern, H., Eskes, H., Hirtl, M., Žabkar, R., Carmichael, G. R., Flemming, J., Inness,  
1140 A., Pagowski, M., Pérez Camaño, J. L., Saide, P. E., San Jose, R., Sofiev, M., Vira, J., Baklanov,  
1141 A., Carnevale, C., Grell, G., and Seigneur, C.: Data assimilation in atmospheric chemistry  
1142 models: current status and future prospects for coupled chemistry meteorology models,  
1143 *Atmospheric Chemistry and Physics*, 15, 5325-5358, 2015.

1144 Bocquet, M. and Sakov, P.: Joint state and parameter estimation with an iterative ensemble Kalman  
1145 smoother, *Nonlinear Processes in Geophysics*, 20, 803-818, 2013.

1146 Basu, S., Guerlet, S., Butz, A., Houweling, S., Hasekamp, O., Aben, I., Krummel, P., Steele, P.,  
1147 Langenfelds, R., Torn, M., Biraud, S., Stephens, B., Andrews, A., and Worthy, D.: Global CO<sub>2</sub>  
1148 fluxes estimated from GOSAT retrievals of total column CO<sub>2</sub>, *Atmospheric Chemistry and*

1149 Physics, 13, 8695-8717, 2013.

1150 Bauwens, M., Compornolle, S., Stavrou, T., Müller, J.-F., van Gent, J., Eskes, H., Levelt, P. F.,  
 1151 van der A, R., Veefkind, J. P., Vlietinck, J., Yu, H., and Zehner, C.: Impact of Coronavirus  
 1152 Outbreak on NO<sub>2</sub> Pollution Assessed Using TROPOMI and OMI Observations, 47,  
 1153 e2020GL087978, 10.1029/2020gl087978, 2020.

1154 Bierman: Factorization methods for Discrete Sequential estimation, Academic Press, 1977.

1155 Binkowski, F. S. and Roselle, S. J.: Models-3 community multiscale air quality (CMAQ) model  
 1156 aerosol component - 1. Model description, Journal of Geophysical Research-Atmospheres, 108,  
 1157 10.1029/2001jd001409, 2003.

1158 Brandhorst, N., Erdal, D., and Neuweiler, I.: Soil moisture prediction with the ensemble Kalman  
 1159 filter: Handling uncertainty of soil hydraulic parameters, Advances in Water Resources, 110,  
 1160 360-370, 2017.

1161 Bruhwiler, L. M. P., Michalak, A. M., Peters, W., Baker, D. F., and Tans, P.: An improved Kalman  
 1162 Smoother for atmospheric inversions, Atmos. Chem. Phys., 5, 2691-2702, 10.5194/acp-5-  
 1163 2691-2005, 2005.

1164 Carlton, A. G., Turpin, B. J., Altieri, K. E., Seitzinger, S. P., Mathur, R., Roselle, S. J., and Weber,  
 1165 R. J.: CMAQ Model Performance Enhanced When In-Cloud Secondary Organic Aerosol is  
 1166 Included: Comparisons of Organic Carbon Predictions with Measurements, Environmental  
 1167 Science & Technology, 42, 8798-8802, 2008

1168 Chen, D., Liu, Z., Ban, J., and Chen, M.: The 2015 and 2016 wintertime air pollution in China: SO<sub>2</sub>  
 1169 emission changes derived from a WRF-Chem/EnKF coupled data assimilation system,  
 1170 Atmospheric Chemistry and Physics, 19, 8619-8650, 10.5194/acp-19-8619-2019, 2019.

1171 Chen, D., Liu, Z., Fast, J., and Ban, J.: Simulations of sulfate-nitrate-ammonium (SNA) aerosols  
 1172 during the extreme haze events over northern China in October 2014, Atmospheric Chemistry  
 1173 and Physics, 16, 10707-10724, 10.5194/acp-16-10707-2016, 2016.

1174 Chevallier, F., Bréon, F.-M., and Rayner, P. J.: Contribution of the Orbiting Carbon Observatory to  
 1175 the estimation of CO<sub>2</sub> sources and sinks: Theoretical study in a variational data assimilation  
 1176 framework, 112, 10.1029/2006JD007375, 2007.

1177 Clements, A. L., Fraser, M. P., Upadhyay, N., Herckes, P., Sundblom, M., Lantz, J., and Solomon,  
 1178 P. A.: Chemical characterization of coarse particulate matter in the Desert Southwest - Pinal  
 1179 County Arizona, USA, Atmospheric Pollution Research, 5, 52-61, 10.5094/apr.2014.007, 2014.

1180 Clements, N., Hannigan, M. P., Miller, S. L., Peel, J. L., and Milford, J. B.: Comparisons of urban  
 1181 and rural PM<sub>10-2.5</sub> and PM<sub>2.5</sub> mass concentrations and semi-volatile fractions in northeastern  
 1182 Colorado, Atmospheric Chemistry and Physics, 16, 7469-7484, 10.5194/acp-16-7469-2016,  
 1183 2016.

1184 Daley, R.: Atmospheric Data Assimilation (gtSpecial Issue>Data Assimilation in Meteorology and  
 1185 Oceanography: Theory and Practice), Journal of the Meteorological Society of Japan. Ser. II,  
 1186 75, 319-329, 1997.

1187 Derber, J. C.: A VARIATIONAL CONTINUOUS ASSIMILATION TECHNIQUE, Monthly  
1188 Weather Review, 117, 2437-2446, 1989.

1189 de Foy, B., Lu, Z., Streets, D. G., Lamsal, L. N., and Duncan, B. N.: Estimates of power plant NOx  
1190 emissions and lifetimes from OMI NO2 satellite retrievals, Atmospheric Environment, 116, 1-  
1191 11, 10.1016/j.atmosenv.2015.05.056, 2015.

1192 De Lannoy, G. J. M., Houser, P. R., Pauwels, V. R. N., and Verhoest, N. E. C.: State and bias  
1193 estimation for soil moisture profiles by an ensemble Kalman filter: Effect of assimilation depth  
1194 and frequency, 43, 2007.

1195 Ding, J., van der A, R. J., Mijling, B., Levelt, P. F., and Hao, N.: NOx emission estimates during the  
1196 2014 Youth Olympic Games in Nanjing, Atmospheric Chemistry and Physics, 15, 9399-9412,  
1197 10.5194/acp-15-9399-2015, 2015.

1198 Elbern, H., Strunk, A., Schmidt, H., and Talagrand, O.: Emission rate and chemical state estimation  
1199 by 4-dimensional variational inversion, Atmospheric Chemistry and Physics, 7, 3749-3769,  
1200 10.5194/acp-7-3749-2007, 2007.

1201 Evensen, G.: The Ensemble Kalman Filter for Combined State and Parameter Estimation MONTE  
1202 CARLO TECHNIQUES FOR DATA ASSIMILATION IN LARGE SYSTEMS, Ieee Control  
1203 Systems Magazine, 29, 83-104, 10.1109/mcs.2009.932223, 2009.

1204 Feng, S., Jiang, F., Jiang, Z., Wang, H., Cai, Z., and Zhang, L.: Impact of 3DVAR assimilation of  
1205 surface PM2.5 observations on PM2.5 forecasts over China during wintertime, Atmospheric  
1206 Environment, 187, 34-49, 10.1016/j.atmosenv.2018.05.049, 2018.

1207 Feng, S., Jiang, F., Wang, H., Shen, Y., Zheng, Y., Zhang, L., Lou, C., and Ju, W.: Anthropogenic  
1208 emissions estimated using surface observations and their impacts on PM2.5 source  
1209 apportionment over the Yangtze River Delta, China, Science of The Total Environment, 828,  
1210 154522, 2022

1211 Feng, S., Jiang, F., Wu, Z., Wang, H., Ju, W., and Wang, H.: CO Emissions Inferred From Surface  
1212 CO Observations Over China in December 2013 and 2017, Journal of Geophysical Research-  
1213 Atmospheres, 125, 10.1029/2019jd031808, 2020a.

1214 Feng, S., Jiang, F., Wang, H., Wang, H., Ju, W., Shen, Y., Zheng, Y., Wu, Z., and Ding, A.: NOx  
1215 Emission Changes Over China During the COVID-19 Epidemic Inferred From Surface NO2  
1216 Observations, Geophysical Research Letters, 47, 10.1029/2020gl090080, 2020b.

1217 Feng, S. and Jiang, F.: Anthropogenic air pollutant emissions over China inferred by Regional multi-  
1218 Air Pollutant Assimilation System (RAPAS v1.0), Zenodo, 10.5281/zenodo.4718290, 2021.

1219 Gaspari, G. and Cohn, S. E.: Construction of correlation functions in two and three dimensions,  
1220 Quarterly Journal of the Royal Meteorological Society, 125, 723-757, 10.1256/smsqj.55416,  
1221 1999.

1222 Guenther, A. B., Jiang, X., Heald, C. L., Sakulyanontvittaya, T., Duhl, T., Emmons, L. K., and Wang,  
1223 X.: The Model of Emissions of Gases and Aerosols from Nature version 2.1 (MEGAN2.1): an  
1224 extended and updated framework for modeling biogenic emissions, Geoscientific Model



- 1225 Development, 5, 1471-1492, 10.5194/gmd-5-1471-2012, 2012.
- 1226 Gurney, K. R., Law, R. M., Denning, A. S., Rayner, P. J., Pak, B. C., Baker, D., Bousquet, P.,  
1227 Bruhwiler, L., Chen, Y. H., Ciais, P., Fung, I. Y., Heimann, M., John, J., Maki, T., Maksyutov,  
1228 S., Peylin, P., Prather, M., and Taguchi, S.: Transcom 3 inversion intercomparison: Model mean  
1229 results for the estimation of seasonal carbon sources and sinks, *Global Biogeochemical Cycles*,  
1230 18, 10.1029/2003gb002111, 2004.
- 1231 He, W., van der Velde, I. R., Andrews, A. E., Sweeney, C., Miller, J., Tans, P., van der Laan-Luijkx,  
1232 I. T., Nehr Korn, T., Mountain, M., Ju, W., Peters, W., and Chen, H.: CTDAS-Lagrange v1.0: a  
1233 high-resolution data assimilation system for regional carbon dioxide observations,  
1234 *Geoscientific Model Development*, 11, 3515-3536, 10.5194/gmd-11-3515-2018, 2018.
- 1235 Hinds, W.C.: *Aerosol Technology: Properties, Behavior, and Measurement of Airborne Particles*.  
1236 New York: John Wiley, 1982.
- 1237 Houtekamer, P. L. and Mitchell, H. L.: A sequential ensemble Kalman filter for atmospheric data  
1238 assimilation, *Monthly Weather Review*, 129, 123-137, 10.1175/1520-  
1239 0493(2001)129<0123:asekff>2.0.co;2, 2001.
- 1240 Houtekamer, P. L. and Zhang, F.: Review of the Ensemble Kalman Filter for Atmospheric Data  
1241 Assimilation, *Monthly Weather Review*, 144, 4489-4532, 10.1175/mwr-d-15-0440.1, 2016.
- 1242 Inness, A., Blechschmidt, A. M., Bouarar, I., Chabrilat, S., Crepulja, M., Engelen, R. J., Eskes, H.,  
1243 Flemming, J., Gaudel, A., Hendrick, F., Huijnen, V., Jones, L., Kapsomenakis, J., Katragkou,  
1244 E., Keppens, A., Langerock, B., de Maziere, M., Melas, D., Parrington, M., Peuch, V. H.,  
1245 Razinger, M., Richter, A., Schultz, M. G., Suttie, M., Thouret, V., Vrekoussis, M., Wagner, A.,  
1246 and Zerefos, C.: Data assimilation of satellite-retrieved ozone, carbon monoxide and nitrogen  
1247 dioxide with ECMWF's Composition-IFS, *Atmospheric Chemistry and Physics*, 15, 5275-5303,  
1248 2015.
- 1249 Jiang, F., Liu, Q., Huang, X., Wang, T., Zhuang, B., and Xie, M.: Regional modeling of secondary  
1250 organic aerosol over China using WRF/Chem, *Journal of Aerosol Science*, 43, 57-73,  
1251 10.1016/j.jaerosci.2011.09.003, 2012a.
- 1252 Jiang, F., Zhou, P., Liu, Q., Wang, T., Zhuang, B., and Wang, X.: Modeling tropospheric ozone  
1253 formation over East China in springtime, *Journal of Atmospheric Chemistry*, 69, 303-319,  
1254 10.1007/s10874-012-9244-3, 2012b.
- 1255 Jiang, F., Wang, H. M., Chen, J. M., Machida, T., Zhou, L. X., Ju, W. M., Matsueda, H., and Sawa,  
1256 Y.: Carbon balance of China constrained by CONTRAIL aircraft CO<sub>2</sub> measurements,  
1257 *Atmospheric Chemistry and Physics*, 14, 10133-10144, 10.5194/acp-14-10133-2014, 2014.
- 1258 Jiang, F., Wang, H., Chen, J. M., Ju, W., Tian, X., Feng, S., Li, G., Chen, Z., Zhang, S., Lu, X., Liu,  
1259 J., Wang, H., Wang, J., He, W., and Wu, M.: Regional CO<sub>2</sub> fluxes from 2010 to 2015 inferred  
1260 from GOSAT XCO<sub>2</sub> retrievals using a new version of the Global Carbon Assimilation System,  
1261 *Atmos. Chem. Phys.*, 21, 1963-1985, 10.5194/acp-21-1963-2021, 2021.
- 1262 Jiang, W., Smyth, S., Giroux, E., Roth, H., and Yin, D.: Differences between CMAQ fine mode  
1263 particle and PM<sub>2.5</sub> concentrations and their impact on model performance evaluation in the

1264 lower Fraser valley, *Atmospheric Environment*, 40, 4973-4985,  
1265 10.1016/j.atmosenv.2005.10.069, 2006.

1266 Jiang, Z., Jones, D. B. A., Worden, H. M., Deeter, M. N., Henze, D. K., Worden, J., Bowman, K. W.,  
1267 Brenninkmeijer, C. A. M., and Schuck, T. J.: Impact of model errors in convective transport on  
1268 CO source estimates inferred from MOPITT CO retrievals, *Journal Of Geophysical Research-  
1269 Atmospheres*, 118, 2073-2083, 2013a.

1270 Jiang, Z., Liu, Z., Wang, T., Schwartz, C. S., Lin, H.-C., and Jiang, F.: Probing into the impact of  
1271 3DVAR assimilation of surface PM10 observations over China using process analysis, *Journal  
1272 of Geophysical Research: Atmospheres*, 118, 6738-6749, 10.1002/jgrd.50495, 2013b.

1273 Jiang, Z., Worden, J. R., Worden, H., Deeter, M., Jones, D. B. A., Arellano, A. F., and Henze, D. K.:  
1274 A 15-year record of CO emissions constrained by MOPITT CO observations, *Atmospheric  
1275 Chemistry And Physics*, 17, 4565-4583, 10.5194/acp-17-4565-2017, 2017.

1276 Jin, J., Lin, H. X., Heemink, A., and Segers, A.: Spatially varying parameter estimation for dust  
1277 emissions using reduced-tangent-linearization 4DVar, *Atmospheric Environment*, 187, 358-  
1278 373, 10.1016/j.atmosenv.2018.05.060, 2018.

1279 Kahnert, M.: Variational data analysis of aerosol species in a regional CTM: background error  
1280 covariance constraint and aerosol optical observation operators, *Tellus B*, 60, 2008.

1281 Kang, J.-S., Kalnay, E., Miyoshi, T., Liu, J., and Fung, I.: Estimation of surface carbon fluxes with  
1282 an advanced data assimilation methodology, 117, 10.1029/2012JD018259, 2012.

1283 Keppenne, C. L., Rienecker, M. M., Kurkowski, N. P., and Adamec, D. A.: Ensemble Kalman filter  
1284 assimilation of temperature and altimeter data with bias correction and application to seasonal  
1285 prediction, *Nonlin. Processes Geophys.*, 12, 491-503, 2005.

1286 Kleist, D. T., Parrish, D. F., Derber, J. C., Treadon, R., Wu, W.-S., and Lord, S.: Introduction of the  
1287 GSI into the NCEP Global Data Assimilation System, *Weather and Forecasting*, 24, 1691-1705,  
1288 10.1175/2009waf2222201.1, 2009.

1289 Kong, L., Tang, X., Zhu, J., Wang, Z., Pan, Y., Wu, H., Wu, L., Wu, Q., He, Y., Tian, S., Xie, Y., Liu,  
1290 Z., Sui, W., Han, L., and Carmichael, G.: Improved Inversion of Monthly Ammonia Emissions  
1291 in China Based on the Chinese Ammonia Monitoring Network and Ensemble Kalman Filter,  
1292 *Environmental Science & Technology*, 53, 12529-12538, 10.1021/acsest.9b02701, 2019a.

1293 Kong, L., Tang, X., Zhu, J., Wang, Z., Fu, J. S., Wang, X., Itahashi, S., Yamaji, K., Nagashima, T.,  
1294 Lee, H. J., Kim, C. H., Lin, C. Y., Chen, L., Zhang, M., Tao, Z., Li, J., Kajino, M., Liao, H.,  
1295 Sudo, K., Wang, Y., Pan, Y., Tang, G., Li, M., Wu, Q., Ge, B., and Carmichael, G. R.: Evaluation  
1296 and uncertainty investigation of the NO<sub>2</sub>, CO and NH<sub>3</sub> modeling over China under the  
1297 framework of MICS-Asia III, *Atmos. Chem. Phys. Discuss.*, 2019, 1-33, 10.5194/acp-2018-  
1298 1158, 2019b.

1299 Laloyaux, P., Bonavita, M., Chrust, M., and Gürol, S.: Exploring the potential and limitations of  
1300 weak-constraint 4D-Var, *Quarterly Journal of the Royal Meteorological Society*, 146, 4067-  
1301 4082, 2020

- 1302 Li, J.-d., Deng, Q.-h., Lu, C., and Huang, B.-l.: Chemical compositions and source apportionment  
1303 of atmospheric PM<sub>10</sub> in suburban area of Changsha, China, *Journal of Central South*  
1304 *University of Technology*, 17, 509-515, 2010.
- 1305 Li, M., Zhang, Q., Kurokawa, J.-i., Woo, J.-H., He, K., Lu, Z., Ohara, T., Song, Y., Streets, D. G.,  
1306 Carmichael, G. R., Cheng, Y., Hong, C., Huo, H., Jiang, X., Kang, S., Liu, F., Su, H., and Zheng,  
1307 B.: MIX: a mosaic Asian anthropogenic emission inventory under the international  
1308 collaboration framework of the MICS-Asia and HTAP, *Atmospheric Chemistry and Physics*,  
1309 17, 935-963, 10.5194/acp-17-935-2017, 2017.
- 1310 Liu, C. and Shi, K.: A review on methodology in O<sub>3</sub>-NO<sub>x</sub>-VOC sensitivity study, *Environmental*  
1311 *Pollution*, 291, 118249, 2021.
- 1312 Liu, Y., Kalnay, E., Zeng, N., Asrar, G., Chen, Z., and Jia, B.: Estimating surface carbon fluxes based  
1313 on a local ensemble transform Kalman filter with a short assimilation window and a long  
1314 observation window: an observing system simulation experiment test in GEOS-Chem 10.1,  
1315 *Geoscientific Model Development*, 12, 2899-2914, 2019.
- 1316 Liu, Z., Liu, Q., Lin, H.-C., Schwartz, C. S., Lee, Y.-H., and Wang, T.: Three-dimensional variational  
1317 assimilation of MODIS aerosol optical depth: Implementation and application to a dust storm  
1318 over East Asia, *Journal of Geophysical Research: Atmospheres*, 116, n/a-n/a,  
1319 10.1029/2011jd016159, 2011.
- 1320 Lorenc, A. C.: Modelling of error covariances by 4D-Var data assimilation, *Quarterly Journal of the*  
1321 *Royal Meteorological Society*, 129, 3167-3182, 2003.
- 1322 Hamer, P. D., Bowman, K. W., Henze, D. K., Attie, J. L., and Marecal, V.: The impact of observing  
1323 characteristics on the ability to predict ozone under varying polluted photochemical regimes,  
1324 *Atmospheric Chemistry and Physics*, 15, 10645-10667, 2015.
- 1325 Ma, C., Wang, T., Mizzi, A. P., Anderson, J. L., Zhuang, B., Xie, M., and Wu, R.: Multiconstituent  
1326 Data Assimilation With WRF-Chem/DART: Potential for Adjusting Anthropogenic Emissions  
1327 and Improving Air Quality Forecasts Over Eastern China, 124, 7393-7412,  
1328 10.1029/2019jd030421, 2019.
- 1329 Meirink, J. F., Bergamaschi, P., and Krol, M. C.: Four-dimensional variational data assimilation for  
1330 inverse modelling of atmospheric methane emissions: method and comparison with synthesis  
1331 inversion, *Atmospheric Chemistry and Physics*, 8, 6341-6353, 2008.
- 1332 Meirink, J. F., Eskes, H. J., and Goede, A. P. H.: Sensitivity analysis of methane emissions derived  
1333 from SCIAMACHY observations through inverse modelling, *Atmospheric Chemistry and*  
1334 *Physics*, 6, 1275-1292, 10.5194/acp-6-1275-2006, 2006.
- 1335 Maybeck: *Stochastic Models, Estimation and Control* Academic Press, 1979.
- 1336 Miyazaki, K. and Eskes, H.: Constraints on surface NO<sub>x</sub> emissions by assimilating satellite  
1337 observations of multiple species, *Geophysical Research Letters*, 40, 4745-4750,  
1338 10.1002/grl.50894, 2013.
- 1339 Miyazaki, K., Eskes, H. J., and Sudo, K.: Global NO<sub>x</sub> emission estimates derived from an

1340 assimilation of OMI tropospheric NO<sub>2</sub> columns, *Atmospheric Chemistry and Physics*, 12,  
1341 2263-2288, 10.5194/acp-12-2263-2012, 2012a.

1342 Miyazaki, K., Eskes, H. J., Sudo, K., Takigawa, M., van Weele, M., and Boersma, K. F.:  
1343 Simultaneous assimilation of satellite NO<sub>2</sub>, O<sub>3</sub>, CO, and HNO<sub>3</sub> data for the analysis of  
1344 tropospheric chemical composition and emissions, *Atmospheric Chemistry and Physics*, 12,  
1345 9545-9579, 10.5194/acp-12-9545-2012, 2012b.

1346 Miyazaki, K., Eskes, H., Sudo, K., Boersma, K. F., Bowman, K., and Kanaya, Y.: Decadal changes  
1347 in global surface NO<sub>x</sub> emissions from multi-constituent satellite data assimilation,  
1348 *Atmospheric Chemistry and Physics*, 17, 807-837, 2017.

1349 Mizzi, A. P., Edwards, D. P., and Anderson, J. L.: Assimilating compact phase space retrievals  
1350 (CPSRs): comparison with independent observations (MOZAIC in situ and IASI retrievals)  
1351 and extension to assimilation of truncated retrieval profiles, *Geoscientific Model Development*,  
1352 11, 3727-3745, 2018.

1353 Monteil, G., Houweling, S., Butz, A., Guerlet, S., Schepers, D., Hasekamp, O., Frankenberg, C.,  
1354 Scheepmaker, R., Aben, I., and Rockmann, T.: Comparison of CH<sub>4</sub> inversions based on 15  
1355 months of GOSAT and SCIAMACHY observations, *Journal of Geophysical Research-*  
1356 *Atmospheres*, 118, 11807-11823, 2013.

1357 Muller, J. F. and Stavrou, T.: Inversion of CO and NO<sub>x</sub> emissions using the adjoint of the  
1358 IMAGES model, *Atmospheric Chemistry and Physics*, 5, 1157-1186, 2005.

1359 Nassar, R., Jones, D. B. A., Kulawik, S. S., Worden, J. R., Bowman, K. W., Andres, R. J.,  
1360 Suntharalingam, P., Chen, J. M., Brenninkmeijer, C. A. M., Schuck, T. J., Conway, T. J., and  
1361 Worthy, D. E.: Inverse modeling of CO<sub>2</sub> sources and sinks using satellite observations of CO<sub>2</sub>  
1362 from TES and surface flask measurements, *Atmospheric Chemistry and Physics*, 11, 6029-  
1363 6047, 2011.

1364 Navon, I. M.: Practical and theoretical aspects of adjoint parameter estimation and identifiability in  
1365 meteorology and oceanography, *Dynamics of Atmospheres and Oceans*, 27, 55-79, 1998.

1366 Parrish, D. F. and Derber, J. C.: The National Meteorological Center's spectral statistical-  
1367 interpolation analysis system, *Monthly Weather Review*, 120, 1747-1763, 10.1175/1520-  
1368 0493(1992)120<1747:tnmc>2.0.co;2, 1992.

1369 Paulot, F., Jacob, D. J., Pinder, R. W., Bash, J. O., Travis, K., and Henze, D. K.: Ammonia emissions  
1370 in the United States, European Union, and China derived by high-resolution inversion of  
1371 ammonium wet deposition data: Interpretation with a new agricultural emissions inventory  
1372 (MASAGE\_NH<sub>3</sub>), *Journal of Geophysical Research-Atmospheres*, 119, 4343-4364, 2014.

1373 Peng, Z., Liu, Z., Chen, D., and Ban, J.: Improving PM<sub>2.5</sub> forecast over  
1374 China by the joint adjustment of initial conditions and source emissions with an ensemble  
1375 Kalman filter, *Atmospheric Chemistry and Physics*, 17, 4837-4855, 10.5194/acp-17-4837-  
1376 2017, 2017.

1377 Peng, Z., Lei, L., Liu, Z., Su, J., Ding, A., Ban, J., Chen, D., Kou, X., and Chu, K.: The impact of  
1378 multi-species surface chemical observation assimilation on air quality forecasts in China,

1379 Atmospheric Chemistry and Physics, 18, 10.5194/acp-18-17387-2018, 2018.

1380 Peters, W., Jacobson, A. R., Sweeney, C., Andrews, A. E., Conway, T. J., Masarie, K., Miller, J. B.,  
1381 Bruhwiler, L. M. P., Petron, G., Hirsch, A. I., Worthy, D. E. J., van der Werf, G. R., Randerson,  
1382 J. T., Wennberg, P. O., Krol, M. C., and Tans, P. P.: An atmospheric perspective on North  
1383 American carbon dioxide exchange: CarbonTracker, Proceedings of the National Academy of  
1384 Sciences of the United States of America, 104, 18925-18930, 10.1073/pnas.0708986104, 2007.

1385 Peylin, P., Rayner, P. J., Bousquet, P., Carouge, C., Hourdin, F., Heinrich, P., Ciais, P., and  
1386 contributors, A.: Daily CO<sub>2</sub> flux estimates over Europe from continuous atmospheric  
1387 measurements: 1, inverse methodology, Atmospheric Chemistry and Physics, 5, 3173-3186,  
1388 10.5194/acp-5-3173-2005, 2005.

1389 Purser, R. J., Wu, W. S., Parrish, D. F., and Roberts, N. M.: Numerical aspects of the application of  
1390 recursive filters to variational statistical analysis. Part I: Spatially homogeneous and isotropic  
1391 Gaussian covariances, Monthly Weather Review, 131, 1524-1535, 10.1175//1520-  
1392 0493(2003)131<1524:naotao>2.0.co;2, 2003.

1393 Quan, J., Liu, Q., Li, X., Gao, Y., Jia, X., Sheng, J., Liu, Y., 2015. Effect of heterogeneous aqueous  
1394 reactions on the secondary formation of inorganic aerosols during haze events. Atmospheric  
1395 Environment 122, 306-312.

1396 Rabier, F., McNally, A., Andersson, E., Courtier, P., Uden, P., Eyre, J., Hollingsworth, A., and  
1397 Bouttier, F.: The ECMWF implementation of three-dimensional variational assimilation (3D-  
1398 Var). II: Structure functions, Quarterly Journal Of the Royal Meteorological Society, 124,  
1399 1809-1829, 10.1256/smsqj.55002, 1998.

1400 Reichle, R. H., McLaughlin, D. B., and Entekhabi, D.: Hydrologic data assimilation with the  
1401 ensemble Kalman filter, Monthly Weather Review, 130, 103-114, 2002.

1402 Richardson, H., Basu, S., and Holtslag, A. A. M.: Improving Stable Boundary-Layer Height  
1403 Estimation Using a Stability-Dependent Critical Bulk Richardson Number, Boundary-Layer  
1404 Meteorology, 148, 93-109, 2013.

1405 Ruiz, J. and Pulido, M.: Parameter Estimation Using Ensemble-Based Data Assimilation in the  
1406 Presence of Model Error, Monthly Weather Review, 143, 1568-1582, 2015.

1407 Sarwar, G., Simon, H., Bhave, P., and Yarwood, G.: Examining the impact of heterogeneous nitril  
1408 chloride production on air quality across the United States, Atmospheric Chemistry and  
1409 Physics, 12, 6455-6473, 10.5194/acp-12-6455-2012, 2012.

1410 Sasaki, Y.: SOME BASIC FORMALISMS IN NUMERICAL VARIATIONAL ANALYSIS,  
1411 Monthly Weather Review, 98, 875-&, 1970.

1412 Schneising, O., Buchwitz, M., Burrows, J. P., Bovensmann, H., Bergamaschi, P., and Peters, W.:  
1413 Three years of greenhouse gas column-averaged dry air mole fractions retrieved from satellite  
1414 - Part 2: Methane, Atmospheric Chemistry and Physics, 9, 443-465, 2009.

1415 Schwartz, C. S., Liu, Z., Lin, H.-C., and Cetola, J. D.: Assimilating aerosol observations with a  
1416 "hybrid" variational-ensemble data assimilation system, Journal Of Geophysical Research-

1417 Atmospheres, 119, 4043-4069, 10.1002/2013jd020937, 2014.

1418 Sekiyama, T. T., Tanaka, T. Y., Shimizu, A., and Miyoshi, T.: Data assimilation of CALIPSO aerosol  
1419 observations, *Atmospheric Chemistry and Physics*, 10, 39-49, 10.5194/acp-10-39-2010, 2010.

1420 Shen, Y., Jiang, F., Feng, S., Zheng, Y., Cai, Z., and Lyu, X.: Impact of weather and emission changes  
1421 on NO<sub>2</sub> concentrations in China during 2014–2019, *Environmental Pollution*, 269, 116163,  
1422 10.1016/j.envpol.2020.116163, 2021.

1423 Shi, X. and Brasseur, G. P.: The Response in Air Quality to the Reduction of Chinese Economic  
1424 Activities During the COVID-19 Outbreak, 47, e2020GL088070, 10.1029/2020gl088070,  
1425 2020.

1426 Stanevich, I., Jones, D. B. A., Strong, K., Keller, M., Henze, D. K., Parker, R. J., Boesch, H., Wunch,  
1427 D., Notholt, J., Petri, C., Warneke, T., Sussmann, R., Schneider, M., Hase, F., Kivi, R.,  
1428 Deutscher, N. M., Velazco, V. A., Walker, K. A., and Deng, F.: Characterizing model errors in  
1429 chemical transport modeling of methane: using GOSAT XCH<sub>4</sub> data with weak-constraint four-  
1430 dimensional variational data assimilation, *Atmospheric Chemistry and Physics*, 21, 9545-9572,  
1431 2021.

1432 Stavrakou, T., Müller, J.-F., Boersma, K. F., De Smedt, I., and van der A, R. J.: Assessing the  
1433 distribution and growth rates of NO<sub>x</sub> emission sources by inverting a 10-year record of NO<sub>2</sub>  
1434 satellite columns, 35, 10.1029/2008gl033521, 2008.

1435 Sun, A. Y., Morris, A., and Mohanty, S.: Comparison of deterministic ensemble Kalman filters for  
1436 assimilating hydrogeological data, *Advances in Water Resources*, 32, 280-292,  
1437 10.1016/j.advwatres.2008.11.006, 2009.

1438 Takagi, H., Saeki, T., Oda, T., Saito, M., Valsala, V., Belikov, D., Saito, R., Yoshida, Y., Morino, I.,  
1439 Uchino, O., Andres, R. J., Yokota, T., and Maksyutov, S.: On the Benefit of GOSAT  
1440 Observations to the Estimation of Regional CO<sub>2</sub> Fluxes, *SOLA*, 7, 161-164,  
1441 10.2151/sola.2011-041, 2011.

1442 Tang, X., Zhu, J., Wang, Z. F., and Gbaguidi, A.: Improvement of ozone forecast over Beijing based  
1443 on ensemble Kalman filter with simultaneous adjustment of initial conditions and emissions,  
1444 *Atmospheric Chemistry And Physics*, 11, 12901-12916, 10.5194/acp-11-12901-2011, 2011.

1445 Tang, X., Zhu, J., Wang, Z. F., Wang, M., Gbaguidi, A., Li, J., Shao, M., Tang, G. Q., and Ji, D. S.:  
1446 Inversion of CO emissions over Beijing and its surrounding areas with ensemble Kalman filter,  
1447 *Atmospheric Environment*, 81, 676-686, 10.1016/j.atmosenv.2013.08.051, 2013.

1448 Wang, C., Lei, L., Tan, Z.-M., and Chu, K.: Adaptive Localization for Tropical Cyclones With  
1449 Satellite Radiances in an Ensemble Kalman Filter, *Frontiers in Earth Science*, 8,  
1450 10.3389/feart.2020.00039, 2020.

1451 Wang, H., Jiang, F., Wang, J., Ju, W., and Chen, J. M.: Terrestrial ecosystem carbon flux estimated  
1452 using GOSAT and OCO-2 XCO<sub>2</sub> retrievals, *Atmospheric Chemistry and Physics*, 19, 12067-  
1453 12082, 2019a.

1454 Wang, N., Lyu, X., Deng, X., Huang, X., Jiang, F., and Ding, A.: Aggravating O<sub>3</sub> pollution due to

1455 NO<sub>x</sub> emission control in eastern China, *Science of The Total Environment*, 677, 732-744,  
1456 2019b.

1457 Wang, Y. H., Hu, B., Ji, D. S., Liu, Z. R., Tang, G. Q., Xin, J. Y., Zhang, H. X., Song, T., Wang, L.  
1458 L., Gao, W. K., Wang, X. K., and Wang, Y. S.: Ozone weekend effects in the Beijing-Tianjin-  
1459 Hebei metropolitan area, China, *Atmospheric Chemistry and Physics*, 14, 2419-2429, 2014.

1460 Wang, Z., Li, Y., Dong, X., Sun, R., Sun, N., and Pan, L.: Analysis on weekend effect of air  
1461 pollutants in urban atmosphere of Beijing, *Journal of University of Chinese Academy of  
1462 Sciences*, 32, 843-850, 2015.

1463 Wang, Z., Wang, W., Tham, Y.J., Li, Q., Wang, H., Wen, L., Wang, X., Wang, T., 2017. Fast  
1464 heterogeneous N<sub>2</sub>O<sub>5</sub> uptake and ClNO<sub>2</sub> production in power plant and industrial plumes  
1465 observed in the nocturnal residual layer over the North China Plain. *Atmospheric Chemistry  
1466 and Physics* 17, 12361-12378.

1467 Wecht, K. J., Jacob, D. J., Sulprizio, M. P., Santoni, G. W., Wofsy, S. C., Parker, R., Boesch, H., and  
1468 Worden, J.: Spatially resolving methane emissions in California: constraints from the CalNex  
1469 aircraft campaign and from present (GOSAT, TES) and future (TROPOMI, geostationary)  
1470 satellite observations, *Atmospheric Chemistry and Physics*, 14, 8173-8184, 2014.

1471 Wu, H., Tang, X., Wang, Z., Wu, L., Li, J., Wang, W., Yang, W., and Zhu, J.: High-spatiotemporal-  
1472 resolution inverse estimation of CO and NO<sub>x</sub> emission reductions during emission control  
1473 periods with a modified ensemble Kalman filter, *Atmospheric Environment*, 236,  
1474 10.1016/j.atmosenv.2020.117631, 2020.

1475 Wu, W. S., Purser, R. J., and Parrish, D. F.: Three-dimensional variational analysis with spatially  
1476 inhomogeneous covariances, *Monthly Weather Review*, 130, 2905-2916, 10.1175/1520-  
1477 0493(2002)130<2905:tdvaws>2.0.co;2, 2002.

1478 Yang, W., Li, J., Wang, W., Li, J., Ge, M., Sun, Y., Chen, X., Ge, B., Tong, S., Wang, Q., and Wang,  
1479 Z.: Investigating secondary organic aerosol formation pathways in China during 2014,  
1480 *Atmospheric Environment*, 213, 133-147, 2019.

1481 Yumimoto, K., Uno, I., Sugimoto, N., Shimizu, A., Liu, Z., and Winker, D. M.: Adjoint inversion  
1482 modeling of Asian dust emission using lidar observations, *Atmospheric Chemistry and Physics*,  
1483 8, 2869-2884, 2008.

1484 Zhang, F., Weng, Y., Sippel, J. A., Meng, Z., and Bishop, C. H.: Cloud-Resolving Hurricane  
1485 Initialization and Prediction through Assimilation of Doppler Radar Observations with an  
1486 Ensemble Kalman Filter, *Monthly Weather Review*, 137, 2105-2125, 10.1175/2009mwr2645.1,  
1487 2009a.

1488 Zhang, L., Chen, Y., Zhao, Y., Henze, D. K., Zhu, L., Song, Y., Paulot, F., Liu, X., Pan, Y., Lin, Y.,  
1489 and Huang, B.: Agricultural ammonia emissions in China: reconciling bottom-up and top-down  
1490 estimates, *Atmospheric Chemistry and Physics*, 18, 339-355, 2018.

1491 Zhang, Q., Streets, D. G., Carmichael, G. R., He, K. B., Huo, H., Kannari, A., Klimont, Z., Park, I.  
1492 S., Reddy, S., Fu, J. S., Chen, D., Duan, L., Lei, Y., Wang, L. T., and Yao, Z. L.: Asian emissions  
1493 in 2006 for the NASA INTEX-B mission, *Atmospheric Chemistry and Physics*, 9, 5131-5153,

- 1494 10.5194/acp-9-5131-2009, 2009b.
- 1495 Zhang, S., Zheng, X., Chen, J. M., Chen, Z., Dan, B., Yi, X., Wang, L., and Wu, G.: A global carbon  
1496 assimilation system using a modified ensemble Kalman filter, *Geosci. Model Dev.*, 8, 805-816,  
1497 10.5194/gmd-8-805-2015, 2015.
- 1498 Zhang, X., Liu, J., Han, H., Zhang, Y., Jiang, Z., Wang, H., Meng, L., Li, Y. C., and Liu, Y.: Satellite-  
1499 Observed Variations and Trends in Carbon Monoxide over Asia and Their Sensitivities to  
1500 Biomass Burning, *Remote Sensing*, 12, 10.3390/rs12050830, 2020.
- 1501 Zheng, B., Tong, D., Li, M., Liu, F., Hong, C., Geng, G., Li, H., Li, X., Peng, L., Qi, J., Yan, L.,  
1502 Zhang, Y., Zhao, H., Zheng, Y., He, K., and Zhang, Q.: Trends in China's anthropogenic  
1503 emissions since 2010 as the consequence of clean air actions, *Atmospheric Chemistry And  
1504 Physics*, 18, 14095-14111, 10.5194/acp-18-14095-2018, 2018.
- 1505 Zheng, B., Zhang, Q., Tong, D., Chen, C., Hong, C., Li, M., Geng, G., Lei, Y., Huo, H., and He, K.:  
1506 Resolution dependence of uncertainties in gridded emission inventories: a case study in Hebei,  
1507 China, *Atmospheric Chemistry and Physics*, 17, 921-933, 2017.